Astronomy & Astrophysics manuscript no. gcm
September 30, 2025

How clear are the skies of WASP-80b?: 3D Cloud feedback on the atmosphere and spectra of the warm Jupiter

Nishil Mehta[1⋆], Vivien Parmentier[1], Xianyu Tan[2], Elspeth K. H. Lee[3], Tristan Guillot[1], Lindsey S. Wiser[4], Taylor J. Bell[5], Everett Schlawin[6], Kenneth Arnold[7], Sagnick Mukherjee[8,9], Thomas P. Greene[10], Thomas G. Beatty[7], Luis Welbanks[11], Michael R. Line[11], Matthew M. Murphy[12], Jonathan J. Fortney[13], and Kazumasa Ohno[14]

[1] Université de la Côte d'Azur, Observatoire de la Côte d'Azur, CNRS, Laboratoire Lagrange, France
[2] Tsung-Dao Lee Institute & School of Physics and Astronomy, Shanghai Jiao Tong University, Shanghai 201210, People's Republic of China
[3] Center for Space and Habitability, University of Bern, Gesellschaftsstrasse 6, CH-3012 Bern, Switzerland
[4] Johns Hopkins Applied Physics Lab
[5] AURA for the European Space Agency (ESA), Space Telescope Science Institute, 3700 San Martin Drive, Baltimore, MD 21218, USA
[6] Steward Observatory, 933 North Cherry Avenue, Tucson, AZ 85721, USA
[7] Department of Astronomy, University of Wisconsin–Madison, Madison, WI 53703, USA
[8] Department of Astronomy and Astrophysics, University of California at Santa Cruz, Santa Cruz, CA 95064, USA
[9] Department of Physics and Astronomy, Johns Hopkins University, Baltimore, MD, USA
[10] IPAC, MC 100-22, California Institute of Technology, 1200 E. California Blvd., Pasadena, CA, 91125, USA
[11] School of Earth and Space Exploration, Arizona State University, Tempe, AZ, USA
[12] Department of Physics and Astronomy, Michigan State University, East Lansing, MI 48824, USA
[13] Department of Astronomy and Astrophysics, University of California, Santa Cruz, CA, USA
[14] Division of Science, National Astronomical Observatory of Japan, 2-12-1 Osawa, Mitaka-shi 1818588 Tokyo, Japan

Received XXX, ; accepted XXX

ABSTRACT

Context. Close-in warm Jupiters orbiting M-dwarf stars are expected to exhibit diverse atmospheric chemistry, with clouds playing a key role in shaping their albedo, heat distribution, and spectral properties.
Aims. We study WASP-80b, a warm Jupiter orbiting an M-dwarf star, using the latest JWST panchromatic emission and transmission spectra to comprehensively characterize its atmosphere, including cloud coverage, chemical composition, and particle sizes, and compare the observations with predictions from general circulation models (GCMs).
Methods. We use a General Circulation Model (GCM), ADAM (ADvanced Atmospheric MITgcm, formerly known as SPARC/MITgcm), combined with the latest JWST data to study the atmosphere of WASP-80b. A cloud module with radiatively active, tracer-based clouds is integrated with the GCM to study the effects on the atmosphere and the spectrum.
Results. Our results indicate that both emission and transmission spectra are well fit by cloudless GCMs. The data appear to be compatible with large cloud particles of any cloud species or KCl clouds of all particle sizes. The Na_2S condensates of radii 0.1 and 1 μm can be ruled out due to the strength of their radiative feedback. This showcases the unique insights that can be obtained from global modelling of exoplanet atmospheres.
Conclusions. Among the expected clouds to form in WASP-80b, we show that only Na_2S clouds forming particles larger than 10μm, KCl clouds of all particle sizes, or strongly depleted $MgSiO_3$ clouds can be compatible with the apparently cloudless emission and transmission spectra. Observations at shorter wavelengths in both emission and transmission could further distinguish between these cloudy scenarios or a truly cloudless atmosphere.

Key words. planets and satellites: atmospheres - methods: numerical - infrared: planetary systems - planets and satellites: composition

1. Introduction

JWST allows us to discover the diversity of exoplanet atmospheres. While past observatories have mainly focused on characterizing hot Jupiters due to their favourable observational metrics, JWST opens the ground to study the population of Jovian planets with temperatures cooler than 1000 K, also known as warm Jupiters. Whereas numerous studies have pointed out the role of 3D atmospheric transport (Showman & Polvani (2011), detailed review in Showman et al. (2020)) and cloud formation in hot Jupiter atmospheres (Charnay et al. 2015; Parmentier et al. 2016, 2021; Roman & Rauscher 2017, 2019; Lines et al. 2019), the different conditions prevailing in warm Jupiters necessitate a thorough exploration of the interactions between clouds, radiative transfer, and atmospheric circulation. Particularly, now that JWST enables the characterisation of both transmission and emission spectra of warm gas giants, such an exploration can be guided by the observations.

Warm gas giants, with equilibrium temperatures of 500–1000 K, are especially interesting because they can host molecules such as water, methane, and carbon dioxide, as well

⋆ nishil.mehta@oca.eu

as clouds from various condensates. Studying them is important for understanding the diversity of planetary atmospheres and the processes that shape them. With JWST now providing both transmission and emission spectra, these planets can be explored in greater detail, revealing how their compositions and structures are influenced by their host stars and formation histories.

WASP-80b is one such warm gas giant. It is Jupiter-size (~0.97 R_J), orbits an M-dwarf (T_* = 4143 K) on a 3.06 day period, leading to an equilibrium temperature of $\approx 820K$ (Triaud et al. 2013). It has been targeted by JWST as part of the MANATEE JWST Guaranteed Time Observations (GTO) program (JWST-GTO-1177 & JWST-GTO-1185). It was observed both because of its favourable observational metrics and to test whether gas giants around M-dwarfs have different formation pathways than gas giants around other stars (Triaud et al. 2023). This is, to date, the best-characterized warm giant, with both emission and transmission spectra observed over the 2.45 to 11 microns range.

WASP-80b has already revealed some of its secrets. In Bell et al. (2023), methane was detected in both the dayside and the limb of the planet, making it one of the most robust methane detections to date. Furthermore, 1D retrieval studies of the dayside emission spectra (Wiser et al. 2025) imply a 3x solar metallicity and slightly sub-solar C/O ratio, consistent with the current bulk population of hot Jupiters. Arnold et. al., in preparation, will analyse and characterise the transmission spectrum in detail. In the optical and near-infrared wavelength regime (<2.5 μm), Jacobs et al. (2023) used data from the Wide Field Camera 3 (WFC3) aboard the Hubble Space Telescope to provide constraints on the presence and properties of atmospheric aerosols. Jacobs et al. (2023) found that aerosol composition varies across the planet. If clouds are present on the dayside, they may extend into deeper layers of the atmosphere, which results in low geometric albedo (A_g < 0.33). Similar results were obtained by Morel et al. (2025); they also studied the eclipse spectrum of WASP-80b obtained with JWST NIRISS/SOSS (0.68–2.83 μm). Using retrievals and 1D cloud models, they reject MnS and silicate clouds while concluding that cloud species with weak-to-moderate near-infrared reflectance, along with soots or low formation-rate tholin hazes, are consistent with the eclipse spectrum.

Interestingly, whereas most of the dayside spectrum appears cloud-free, grid-based atmospheric retrievals point to a homogeneous, grey cloud to reduce the planetary emission around 4.3 and 10 microns. The 1D grid-based retrieval of Wiser et al. (2025) suggests a high internal effective temperature (T_{int}) of 381^{+38}_{-39} K and vertical quenching of CH_4 with log(K_{zz})=9.13 cm^2s^{-1} to explain the observed reduced CH_4 abundance, similar to the inference in the warm exoplanet WASP-107b (Sing et al. 2024; Welbanks et al. 2024). However, when clouds are assumed to be completely absent from the atmosphere, the grid-based retrieval favours a lower T_{int} (around 250 K) and a higher metallicity ([M/H]=1.15). As a consequence, the presence or absence of clouds in WASP-80b has direct implications for the measurement of its bulk elemental abundances.

The presence of clouds should be ubiquitous for planets in the 500 K to 1000 K temperature range. Indeed, within this range, KCl and Na_2S clouds are expected to condense (Fig. 1: Top Left). If the T_{int} is high enough, silicate clouds can also condense in the deep atmospheric layers (Fig. 1: Bottom Left). However, the observational effect of clouds depends strongly on their spatial distribution, which is determined by the balance between vertical settling and 3D atmospheric mixing. Even though a grey homogeneous cloud opacity can be favoured in 1D retrieval models, it is unclear whether such clouds may indeed exist, given the complex interactions between 3D mixing and settling.

Clouds are expected to play a crucial role in interpreting our observations of exoplanet atmospheres. First, they affect the energy balance of the atmosphere in a complex way; dayside clouds tend to cool the atmosphere by increasing the albedo, whereas nightside clouds tend to increase the temperature of the atmosphere and reduce the day-to-night heat transport through their greenhouse effect. At the same time, nightside clouds raise the photosphere to higher, colder layers of the atmosphere, which lowers the apparent brightness temperature. Clouds can further bias our inference of atmospheric abundances. As shown by Line & Parmentier (2016), the presence of inhomogeneous clouds at the limb can mimic the effect of a high mean-molecular-weight atmosphere. The presence of inhomogeneous clouds at the terminator of warm giant planets was recently confirmed observationally by Murphy et al. (2024). Finally, clouds, even if they form in regions that are not observable directly (e.g., deeper than the photosphere or on the planetary nightside), can sequester specific elements and affect our determination of bulk elemental abundance ratios, such as C/O.

GCMs are necessary to perform a comprehensive analysis of the planet's atmosphere because they can simulate the complex interactions between radiation and dynamics. The 3D structure of the planet makes the process of characterizing the exoplanet atmosphere from its spectra challenging. The atmospheric properties can vary on different parts of the planets, which is usually averaged in observed spectra. With the transmission and emission available for WASP-80b, a GCM will be a perfect tool to study the global atmosphere.

For this, we perform 3D global circulation models (GCMs) of WASP-80b with radiatively active cloud tracers with the ADAM framework (previously known as SPARC/MITgcm). Compared to previous studies for these kinds of planets, we can benchmark our modelling framework on the high-quality emission and transmission spectra (Section 2.1). We present our methods in Section 2, discuss the cloudless case in Section 3, the effect of clouds on the atmospheric dynamics of WASP-80b in Section 4, compare our results to observations by JWST in Section 4.4 and, finally, conclude on the possible cloud species present in WASP-80b atmosphere in Section 5.

2. Methods

In this section, we discuss the data used in this study and describe the GCM, cloud implementation in the GCM, the post-processing, and the convergence criterion for GCMs.

2.1. Data

Both transmission and emission spectra of WASP-80b were observed with the NIRCam and MIRI instruments on board JWST, providing continuous spectra from 2.45 to 14 microns. They consist of NIRCam F322W2 (taken 2022 Oct 29; JWST-GTO-1185 Observation 4), NIRCam F444W (taken 2023 Jun 13; JWST-GTO-1185 Observation 5), and MIRI LRS (taken 2022 Sep 25; JWST-GTO-1177 Observation 2). In this paper, we use the emission spectra published in Wiser et al. (2025) and the transmission spectra that will be published in Arnold et. al., in preparation.

These observations led to the detection of the major carbon and oxygen-bearing species expected in an H_2-dominated atmosphere at these temperatures. CH_4, CO, CO_2, H_2O, and possibly NH_3 are expected in both emission and transmission spectra,

with CS_2 potentially observed only in transmission. The presence or absence of clouds could not be constrained with high confidence. From the emission spectrum, the dayside effective temperature was estimated to be $T_{day} = 859.9^{+7.1}_{-9.1} K$, corresponding to a heat redistribution parameter $f = T_{day}/T_{eq} = 1.04$ (Roth et al. 2024) (see Section 3 for more details).

2.2. Abundances

Warm Jupiters are less likely to follow thermochemical equilibrium compared to hot Jupiters, primarily due to their lower atmospheric temperatures. At these cooler temperatures, chemical reaction rates are significantly slower, allowing disequilibrium processes such as vertical mixing and photochemistry to dominate the chemical composition (Mukherjee et al. 2025). In contrast, the higher temperatures in hot Jupiters allow faster reaction rates, enabling the atmosphere to maintain equilibrium despite dynamical transport. As a result, species such as CH_4, CO, NH3, and HCN in warm Jupiter atmospheres often show deviations from equilibrium predictions (Drummond et al. 2020; Zamyatina et al. 2022, 2024; Lee et al. 2023).

Wiser et al. (2025) and Arnold et. al., in preparation, worked on the emission and transmission dataset of WASP-80b from the MANATEE JWST GTO program. In order to reduce the parameter space to be explored with our models, we decided to set the chemical abundances in the model following the atmospheric retrieval work of Wiser et al. (2025) with metallicity of 0.55 and C/O of 0.48. This was performed using a grid of scCHIMERA models (recently presented in detail in (Iyer et al. 2023; Wiser et al. 2024)), solving for the 1D radiative/convective equilibrium including photochemistry and disequilibrium chemistry through the VULCAN code (Tsai et al. 2021). The best-fit model from Wiser et al. (2025) suggests chemical abundances that vary with pressure. We further assume that the horizontal mixing leads to horizontally homogeneous abundances, and thus we apply the 1D vertically varying abundance at every GCM column. Since the clouds are implemented in the form of tracers, the gas-phase and condensates, for the clouds that are implemented, can be inhomogeneous.

2.3. Opacity

The original setup of ADAM uses a pre-computed k-coefficient table that assumes equilibrium chemistry from Lupu et al. (2021) by calculating the correlated-k coefficients using pre-mixed opacities for each metallicity-C/O combination, as described in Marley et al. (2021). Given the need to use disequilibrium chemistry abundances, we developed a new module to pre-compute k-coefficient opacity tables for arbitrary chemistry inputs.

This module calculates the opacity table by mixing the correlated-k tables according to given abundances, which is then used in the GCM as the opacity of the atmosphere. The correlated-k tables are obtained from Freedman et al. (2014); Gharib-Nezhad et al. (2024). These corr-k tables have a P and T grid similar to Gharib-Nezhad et al. (2024) and have already been implemented in Mukherjee et al. (2024, 2025). The *exo_k* is a Python library to handle radiative opacities from various sources for atmospheric applications. *exo_k* is used to bin down the opacity to 11 bins as in Kataria et al. (2016). We binned down the k-tables using *exo_k* (Leconte 2021). These binned down opacity tables are then mixed according to the abundances of the best-fit model from Wiser et al. (2025).

The random overlap method from Lacis & Oinas (1991) is used to mix the opacity tables. k-coefficients are computed individually for each gas, and k-coefficients for different gases are combined assuming that the absorption coefficient of one gas i, is uncorrelated to that of a second gas j, i.e., that their lines are randomly overlapping. The total transmission of the gas mixture over some column density (u_i, u_j) is then given by a simple scalar product.

$$\mathcal{T}(u_i, u_j) = \mathcal{T}_i(u_i) \times \mathcal{T}_j(u_j). \quad (1)$$

Detailed equations and validity of random overlap have been tested in the atmospheres of hot Jupiter and brown dwarfs in Amundsen et al. (2017). The opacity table mixed by *exo_k* is then fixed as the opacity of the atmosphere for the GCM.

2.4. Internal effective temperatures

Like Jupiter, irradiated giant planets contract and cool; external irradiation experienced by hot or warm Jupiters can slow the cooling but not halt it, due to the development of a radiative zone in the planet's deep atmosphere (Guillot et al. 1996). Atmospheric models must therefore account for both the incoming stellar irradiation and the intrinsic flux due to the planet's cooling. The latter is measured in terms of an internal effective temperature T_{int}, corresponding to a heat flux at thermal wavelengths σT_{int}^4. While standard models generally predict a value of T_{int} close to 100 K (the Jupiter value) for planets of Jupiter's mass and radius, it has been noticed that higher values are required for a number of so-called hot Jupiters (Guillot & Showman 2002). A number of processes have been invoked to explain the mismatch (e.g. Fortney et al. 2021; Guillot et al. 2023), the most known being the interaction between winds in a partially ionized atmosphere and the magnetic field of a tidally locked planet, a process known as ohmic dissipation (Batygin & Stevenson 2010). A parametric study to reproduce on average the sizes of transiting hot and warm Jupiters lead to values ranging from $T_{int} = 100$ K for low-irradiation planets with $T_{eq} = 800$ K to up to $T_{int} = 700$ K for hot Jupiters with $T_{eq} = 1800$ K (Thorngren et al. 2019).

Given WASP-80b's relatively low T_{eq} value, we would expect a value of T_{int} towards the lower range of these values. We therefore adopt $T_{int} = 100$ K as our baseline model. However, given the uncertainties in our knowledge of the inflation mechanism and since some atmospheric retrievals point to higher values, we adopt $T_{int} = 381$ K (see Wiser et al. 2025) as a second possibility.

2.5. General Circulation Model

We use ADAM (ADvanced Atmospheric MITgcm, formerly known as SPARC/MITgcm) (Showman et al. 2019) to simulate the atmosphere for WASP-80b. This model couples the MITgcm, a General Circulation Model maintained at Massachusetts Institute of Technology (Adcroft et al. 2004), and the plane-parallel radiative transfer code of (Marley & McKay 1999) and solves the primitive equations on a cube-sphere grid.

This model has been successfully applied to a wide range of exoplanets, including hot Jupiters (Showman et al. 2009, 2015; Liu & Showman 2013; Parmentier et al. 2016, 2018, 2021; Kataria et al. 2015, 2016; Lewis et al. 2017; Steinrueck et al. 2019; Tan & Showman 2021a), highly eccentric hot Jupiters (Kataria et al. 2013; Lewis et al. 2014), warm Jupiters (Showman et al. 2015) and super-Earths (Kataria et al. 2014; Zhang et al. 2017).

We initialised all the GCMs with the parameters from Table 1, unless stated otherwise. The temperature profile was initialized using the analytical model of Parmentier et al. (2015) that uses the analytical expression of Parmentier & Guillot (2014) adjusted to represent the global average temperature profile of solar-composition atmospheres (Fortney et al. 2007). The simulations did not incorporate any explicit Rayleigh drag-in, as discussed in Showman et al. (2009).

GCM Parameters	
Reference surface pressure [bar]	200
Pressure range	200 bar - 2 μbar
Upper boundary pressure [bar]	10^{-6}
Specific heat capacity c_p [J kg^{-1} K^{-1}]	1.3×10^4
Adiabatic coefficient [κ]	0.286
Gravity g [m s^{-2}]	13.96
Semi-major axis [AU]	0.034
Planetary radius R_p [m]	6.79×10^7
Eccentricity e	0
Orbital period [days]	3.0678
$\log_{10}$ [metallicity]	0.55
Hydrodynamic timestep [s]	40

Table 1. General circulation model (GCM) parameters used in this study. We use a cubed sphere resolution of C32 (128 × 64 in longitude × latitude). There are 53 levels of pressure, giving each scale height nearly three levels of resolution.

2.6. Clouds

Clouds are included in the GCMs in the form of tracers. These tracer-based clouds are radiatively active and evolve according to the local temperature and pressure. The tracers move in the atmosphere according to the atmospheric circulation. The tracers are then given the properties of the specific cloud species, such as condensation curve, density, molecular weight, refractive indices, and Mie parameters (Batalha & Marley 2020). All the cloud species are initialized with the solar abundance scaled to the metallicity of the planet. The radiative feedback of clouds is implemented in the model by computing their optical properties (optical depth, single scattering albedo, and asymmetry factor) from Mie efficiency data (Batalha & Marley 2020) (Na_2S: Montaner et al. (1979); Khachai et al. (2009); KCl: Querry (1987); $MgSiO_3$: Scott & Duley (1996)). These properties are then included in the radiative transfer scheme, allowing clouds to interact with radiation and modify the heating rates. The cloud properties are given in Table 2. Figure A.1 presents the cloud single scattering albedo, extinction, and absorption opacities normalized per unit mass.

We couple the primitive equations of motion to tracer equations for the transport of condensible vapour and cloud condensate by following the method of Tan & Showman (2021a,b):

$$\frac{dq_v}{dt} = (1-\delta)\frac{\min(q_s - q_v, q_c)}{\tau_c} - \delta\frac{(q_v - q_s)}{\tau_c} - \frac{q_v - q_{\rm deep}}{\tau_{\rm deep}}, \quad (2)$$

$$\frac{dq_c}{dt} = \delta\frac{(q_v - q_s)}{\tau_c} - (1-\delta)\frac{\min(q_s - q_v, q_c)}{\tau_c} - \frac{\partial\left(q_c\langle V_p\rangle\right)}{\partial p}. \quad (3)$$

where, q_v is the mass mixing ratio of condensible vapour relative to the background air, q_c is the mass mixing ratio of cloud condensate particles, q_s is the mass mixing ratio of condensible vapour at saturation, δ is the supersaturation indicator, which is set to one when vapour is super-saturated and zero if vapour is sub-saturated, τ_c is the cloud and condensible vapour tracer relaxation timescale, the deep vapour mass mixing ratio $q_{\rm deep}$, and the deep vapour replenishment timescale $\tau_{\rm deep}$. The particle size of the clouds has a log-normal size distribution. The terminal settling velocity in pressure coordinates that is averaged over the particle size distribution $\langle V_p\rangle$. The mean particle size is given as an input to the GCM. For a given particle size, the cloud settling velocity V_s as a function of pressure and temperature is calculated using Eqs. (3-7) of Parmentier et al. (2013).

Adding clouds to ADAM was done in the same way as Tan & Showman (2021a,b). The cloud module of ADAM has already been applied in Komacek et al. (2022) for a two-stream double-gray radiative transfer scheme, whereas we apply it using a non-gray radiative transfer.

As seen in Fig. 1, the condensation curves of Na_2S and KCl cross the pressure-temperature profile. Hence, these clouds are included. And following the results of Wiser et al. (2025), we include $MgSiO_3$ clouds as discussed in the introduction. The condensation curve of Na_2S (Eq. 28 from Visscher et al. (2006)), KCl (Eq. 20 from Morley et al. (2012)) and $MgSiO_3$ (Eq. 20 from Visscher et al. (2010)):

$$10^4/T_{\rm cond}(Na_2S) \approx 10.05 - 0.72 log_{10}P_T - 1.08[M/H] \quad (4)$$

$$10^4/T_{\rm cond}(KCl) \approx 12.479 - 0.879 log_{10}P_T - 0.879[M/H] \quad (5)$$

$$10^4/T_{\rm cond}(MgSiO_3) \approx 6.26 - 0.35 log_{10}P_T - 0.7[M/H] \quad (6)$$

where, $T_{\rm cond}$ is equilibrium condensation temperature, P_T is total gas pressure, and $[M/H]$ is the metallicity of the atmosphere.

We calculated the total gas pressure from the condensation curves. When the local conditions are cooler than the condensation temperature of the cloud species, the gas condenses into clouds. Due to this temperature dependence, clouds are usually expected in the cooler regions of the planet. Instead of calculating the partial pressure of each condensation species tracer and comparing it to the saturation vapour pressure, we directly compare the mass mixing ratio of condensate to the local saturation mass mixing ratio , following Tan & Showman (2019).

$$q_s = P_T \times q_{\rm deep}/p \quad (7)$$

When the condensible vapour mixing ratio is higher than the required saturation mixing ratio, q_s, a cloud forms; otherwise, when the vapour mixing ratio is less than q_s, evaporation takes place. The condensation point depends on the local condensing vapor. The saturation mixing ratio is assumed to be a function of pressure and temperature, so q_s is $q_{\rm deep}$ at the condensation pressure ($p_{\rm cond}$) with a steep decrease when pressure is less than $p_{\rm cond}$. At pressures larger than $p_{\rm cond}$, q_s is assumed to be arbitrarily large such that no condensation would occur. The vapour field is relaxed towards $q_{\rm deep}$ with a time-scales shown in Table 2.

We find instabilities in the GCMs caused by the strong feedback of $MgSiO_3$, leading to unstable convection regions. Following Roman & Rauscher (2019); Lines et al. (2019), we reduced the opacity of $MgSiO_3$ clouds by a factor of 1000 by limiting the amount of gas-phase tracers to 2.7×10^{-6} (as mentioned in Table 2). The distribution of the clouds remains the same, as no

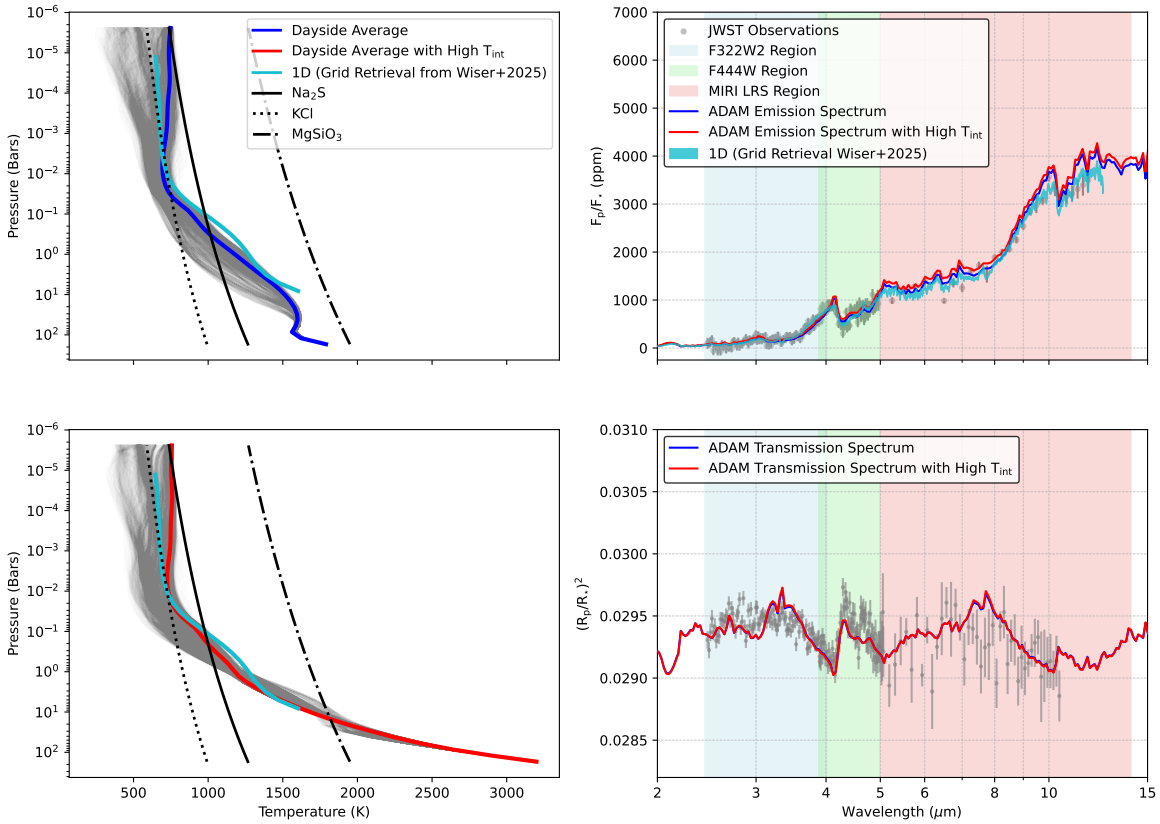

Fig. 1. Left Column: Pressure-temperature profiles from the Cloudless GCM models (top: cloudless GCM with low T_{int}; bottom: cloudless GCM with high T_{int}; gray: profiles at all latitudes and longitudes; light blue: 1D profile from Wiser et al. (2025)). The condensation curves of several important species are plotted as dashed lines. Right Column: ADAM Spectrum plotted with JWST observations in grey (top: emission spectra for cloudless GCM with low and high T_{int} showing significant overlap, indicating minimal sensitivity to internal heating in the terminator region, plotted along with 1D spectrum from Wiser et al. (2025); bottom: transmission spectra for cloudless GCM with low and high T_{int} showing significant overlap, indicating minimal sensitivity to internal heating in the terminator region)

changes are made in the condensation curve (given by Eq. 6 with [M/H]=0.55).

The deep layers of our models reach the unstable convective region. The effects of rapid convective mixing, using a simple convective adjustment scheme as in the NCAR Community Atmosphere Model (Collins et al. (2004), see their Section 4.6), were parametrized. In a vertical atmospheric column, any two adjacent layers that are unstable are instantly converted to a neutral convective condition while still conserving the total sensible heat $\sum \Delta pT$, where Δp is the pressure-dependent layer thickness. The entire column is periodically scanned in a single dynamical step until convective instability is removed everywhere. During adjustment, tracers are also uniformly distributed over the modified domain. The horizontal direction is not adjustable. The GCM models do not include an upper sponge layer, which is typically used to minimize the effects of wave reflection from the upper boundary on dynamics at levels of interest. The physical phenomenon seen in our results and conclusions of this study should be independent of the numerical setup of the numerical diffusion, as shown in Tan & Showman (2021a).

2.7. Post-processing

The post-processing of the GCMs is done using the *gcm_toolkit* code. *gcm_toolkit* is an open-source Python package to read, post-process, and plot 3D GCM data. This package has already been implemented for GCM studies for exoplanets in Carone et al. (2020); Schneider et al. (2022). The gcm-toolkit regrids the output to a regular latitude-longitude grid with the same number of layers: 53. The new latitude-longitude grid is regridded to (45, 72). The output of gcm-toolkit is then used as an input to the 3D radiative transfer code *gcm_toolkit*.

gCMCRT is a 3D GPU-accelerated Monte Carlo Radiative Transfer (Lee et al. 2022) is used on a spherical geometry grid to post-process the GCM results. *gCMCRT* has been previously used along with ADAM at low resolution (Komacek et al. 2022) and high resolution (Wardenier et al. 2021). The effects of cloud structures on the resulting transmission spectra, emission spectra of the model output are studied using *gCMCRT*. *gCMCRT* simulates the path of photon packets through a planetary atmosphere in 3D. It is a hybrid MCRT and ray-tracing code, using the "peel-off" ray-tracing method to produce images and spectra of the simulated planet.

Cloud Properties			
	Na_2S	**KCl**	**$MgSiO_3$**
Condensate vapour deep mixing ratio (q_{deep})	$5.9 \times 10^{-5} \times 10^{[Z]}$	$7.13 \times 10^{-6} \times 10^{[Z]}$	0.0027/1000
Condensate vapour source pressure (p_{deep})	10^7	10^7	3.3×10^7
Condensate vapour deep relaxation timescale (τ_{deep})	1000 s	1000 s	100 s
Condensate density (ρ_c) (Roman et al. 2021)	1860 kg/m^3	1980 kg/m^3	3190 kg/m^3
Mean particle size (r_0)	[0.1, 1, 5, 10] μm	[0.1, 1, 5, 10] μm	[0.1, 1, 5, 10] μm
Log-normal distribution width (σ)	1.65	1.65	1.65
Internal effective Temperature T_{int} (K)	100	100	381

Table 2. Input parameters for cloud microphysics in the GCM simulations. The listed T_{int} reflect those used in the initialization of the GCM model. Metallicity is represented by [Z], with a value of 0.55 for WASP-80b. (Batalha & Marley 2020) (Na_2S: Montaner et al. (1979); Khachai et al. (2009); KCl: Querry (1987); $MgSiO_3$: Scott & Duley (1996))

Previous post-processing of GCMs was usually done by using a plane-parallel code and produced a planetary flux per unit surface, which is then scaled by the measured planetary radius in transit. On the contrary, *gCMCRT* outputs the total outgoing flux, and for gas giant planets, there is no satisfactory definition of surface to normalise the flux. However, an error in the planetary radius would directly translate into an error in the outgoing flux; we therefore need to make sure our model has the correct radius. It is important to note that the radius can be used as a free parameter after the spectrum is obtained. But in this case, the radius of the planet and corresponding reference pressure are calculated by fitting the transmission spectrum of the planet to the observations.

The GCM usually takes as input the radius at 200 bar, which we take as the observed planetary radius. Although this is inaccurate, the atmospheric dynamics of the atmosphere is not strongly dependent on small changes in radius. However, when computing the emission spectra, the error on the planetary size is larger than the JWST error bars. As a consequence, for the emission spectra calculation, we need to benchmark the planetary radius. For this, we calculate a transit spectrum with *gCMCRT* with our initial 200 bar radius (0.97 R_J). We then determine the radius difference between the observed and modelled radius and adjust our 200 bar radius accordingly, so that the calculated transit spectra match the observations. This results in a radius of 0.92 R_J is the 200 bar radius that is then used to calculate the emission spectra. This radius is fixed for the rest of the study, unless otherwise stated. The use of an accurate radius is important as no Photospheric Radius Correction factor $(R_p/R_s)^2$ (Fortney et al. 2019) was used. *gCMCRT* avoids this factor by directly accounting for the volume of the emitting regions. *gCMCRT* correctly weighs the contribution of different temperatures to the spectrum, avoiding known biases (Feng et al. 2016; Taylor et al. 2021).

We also use *gCMCRT* to post-process the GCMs with clouds. We parametrize a log-normal cloud particle size distribution in our GCM as

$$\frac{dn_c}{dr} = \frac{n_c}{\sqrt{2\pi}\sigma r} e^{-[\ln(r/r_0)]^2/(2ln(\sigma)^2)}, \quad (8)$$

where n_c is the cloud particle number per dry air mass, r_0 is the mean particle size, σ is the log-normal distribution width, and n_c is the number of cloud particles per dry air mass, calculated as

$$n_c = \frac{3\rho q_c}{4\pi\rho_c r_0^3 e^{(4.5(ln(\sigma))^2)}} \quad (9)$$

where ρ is the density of the atmosphere.

Our assumed cloud particle size distribution affects the vertical settling of particles through the sink term for cloud condensate on the right hand side of Eq. (3), $-\frac{\partial(q_c\langle V_p\rangle)}{\partial p}$, in which the mean terminal velocity is obtained from proper averaging over the size distribution in Eq. (8).

2.8. Convergence Test

The duration of each simulation was 1000 days. A fully converged state would require thousands of days for the models to be integrated (Mendonça et al. 2018; Mendonça 2020; Wang & Wordsworth 2020). This has several consequences. First, because the integration period is too short, the results cannot be affected by the deep boundary condition we chose. The second is that there is insufficient integration time for a deep circulation to emerge and significantly affect the photospheric level (Mayne et al. 2017; Sainsbury-Martinez et al. 2019; Carone et al. 2020; Wang & Wordsworth 2020). However, at photospheric levels, a pseudo-steady state is achieved (Showman et al. 2009). Assuming that the deep flow does not substantially alter the equilibrium of photospheric levels, this steady state is accurate. To test the convergence of the model, we use the net flux at the top of the atmosphere (TOA) as a convergence criterion. The outgoing flux must be equal to the incoming flux. The model is assumed to have reached a pseudo-steady state when the net flux converges to the equilibrium temperature of the planet. For this test, we use different initial temperature-pressure profiles (T_{eq}=625 K, 800 K, 825 K, 850 K) to show that the GCMs converge to the equilibrium temperature of the planet irrespective of the initial conditions. The convergence test is shown in Fig. 2. The test shows that the model converges to the equilibrium temperature of the planet in less than 1000 days. Fig. 2 shows that there is only a small flux difference after 1000 days.

3. Cloudless GCMs

We use ADAM to model the cloudless atmosphere of WASP-80b, using molecular abundances from Wiser et al. (2025). These abundances were derived from 1D radiative-convective-photochemical equilibrium (RCPE) models and provide a chemically consistent baseline for the 3D GCM.

Figure 1 compares the thermal structure of WASP-80b in two cloudless scenarios: one with a low T_{int} and another with a high T_{int}. In the low T_{int} case, the dayside-nightside temperature contrast at the top of the atmosphere reaches about 250 K, but this contrast diminishes rapidly with depth and drops below 50 K around 0.05 bar. Below that, the atmosphere becomes

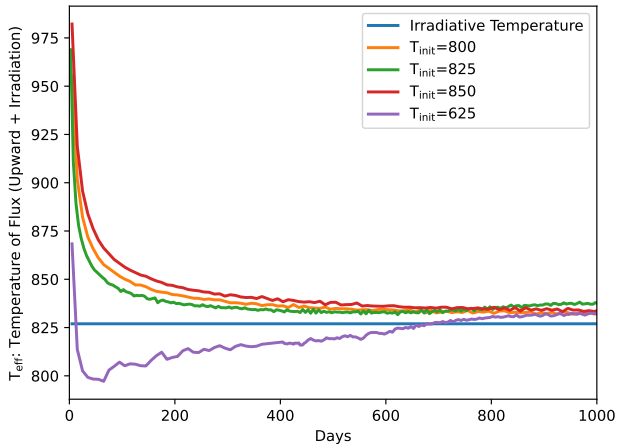

Fig. 2. Effective temperature calculated from global outgoing flux as a function of simulation time for different initial temperature-pressure profiles (T_{eq} = 625, 800, 825, and 850 K). The convergence of all cases toward the same equilibrium flux demonstrates that the GCM solution is independent of the initial conditions.

nearly horizontally uniform in temperature, suggesting efficient heat redistribution.

In the cloudless high T_{int} case, the overall thermal structure remains broadly similar, but the dayside temperatures in the upper atmosphere are slightly warmer. The extra internal heat has only a minor effect on the global thermal distribution, and the day-night contrast remains the same. The terminator regions also show temperature asymmetries of less than 150 K in both cases, indicating longitudinal variation at the limb (Fu et al. 2025).

The differences in atmospheric dynamics become more apparent when comparing the zonal wind structures (Figure 3). In the low T_{int} case, the winds are uniformly prograde across all latitudes. The circulation is dominated by a strong equatorial super-rotating jet and weaker high-latitude jets. This wind pattern is consistent with previous studies of tidally locked hot Jupiters, where thermal gradients drive equatorial jets through eddy momentum transport (Showman & Polvani 2011).

In contrast, the high T_{int} case exhibits a more complex wind structure. While the equatorial super-rotating jet still forms, the high-latitude winds reverse direction and become retrograde, breaking the global prograde symmetry seen in the lower T_{int} case. This shift may be linked to enhanced vertical motions. As shown in Fig. 3, the high T_{int} case develops a pronounced upwelling region on the dayside. This vertical motion could modify angular momentum transport, ultimately leading to the observed polar flow reversal.

3.1. Comparison with the Observations

As shown in Fig. 1, the cloudless GCM matches very well the emission spectrum of the planet, with a χ^2_{red} value of 1.97. This is remarkable for a model as complex as a global circulation model without any fine-tuning of the parameters. It validates both the modelling framework and our approach to use the retrieved chemical abundances from 1D retrieval as input for the 3D model. In terms of dynamics, the agreement of the overall level of dayside flux means that the model properly captures the heat transport in WASP-80b, with a heat redistribution parameter of $f = 1.04$ ($f = (T_{day}/T_{eq})^4$) corresponding to an efficient heat transport (Roth et al. 2024). T_{day} represents the temperature of a blackbody that emits the same total energy as the planet's dayside. Based on this definition, the redistribution factor (commonly referred to as the f-factor) ranges from a minimum of $f = 1$, which corresponds to complete heat redistribution across the entire planet—resulting in uniform temperatures between the day and night sides to a maximum of $f = 2.66$, which represents no heat redistribution, with all incoming energy emitted from the dayside alone. An intermediate value, $f = 2$, represents a theoretical case where heat is redistributed only across the dayside but not to the nightside.

We now compare in Fig. 1 the spectrum and thermal profiles of the 1D grid-retrieval of Wiser et al. (2025) with our cloudless 3D GCM output. We observe some differences in the temperature-pressure (T-P) profiles when comparing the 1D-RCPE (ScCHIMERA) with the 3D-GCM (ADAM). These discrepancies highlight the importance of multidimensional effects—such as atmospheric dynamics and horizontal heat transport, which are inherently captured in 3D models but absent in 1D frameworks. The transport-dominated region ($> 10^{-1}$ bar) in the 3D model shows cooler temperatures due to efficient horizontal heat redistribution, while the photospheric layers (around 10^{-2} bar) exhibit good agreement between the two models. At lower pressures ($< 10^{-1}$ bar), the 3D model tends to be warmer, maintaining radiative balance with deeper layers.

The major differences that are observed between the spectra are around 4 and 10 μm, when compared to the 1D spectrum from Wiser et al. (2025). The 4 μm peak is overestimated by the GCM, whereas in 1D, a grey opacity has been included to obtain a better fit to the data. This grey opacity can be attributed to clouds or molecules such as PH_3. If the grey opacity is considered to be from the clouds, the inferred T_{int} becomes highly sensitive to their presence and properties, as discussed in the introduction. In the cloudless GCM case, deeper layers are visible, making high internal effective temperatures incompatible with the observed 4-4.5 μm flux. The differences around 10 μm are due to the higher temperature from the GCM in the upper atmosphere. The corresponding transmission spectrum slightly overestimates the CH_4 abundance, which can be seen at 3.3 and 7.8 μm features. This overestimation can be due to small changes in the CH_4 abundance between dayside and limbs. If the planet has a high T_{int}, then CH_4 can be quenched in the deeper atmosphere. It should be noted that no differences are observed in the transmission spectra of low and high T_{int}; this is because chemistry is not included in the GCM. Another possibility can be CH_4 being destroyed from the upper atmosphere due to photochemistry. The cloudless GCM model is also a very good fit to the transit spectrum with a χ^2_{red} of 2.75. If we neglect the 4.6 μm feature, which is likely due to photochemistry, the χ^2_{red} goes down to 2.67.

4. Cloudy GCMs

To understand the role of clouds in shaping the atmosphere, we implement clouds in the GCM as radiatively active tracers that interact with both the thermal structure and the winds. Clouds, which are expected to form in the relatively cool environment of this 820 K warm Jupiter, play a dual role: they are influenced by the large-scale circulation and, in turn, significantly impact the planet's thermal profile and wind dynamics. This radiative feedback is particularly important; it can alter the spectra. In the following sections, we explore how the inclusion of clouds modifies the atmospheric structure and circulation patterns, providing physical insight into the observed JWST spectra of WASP-

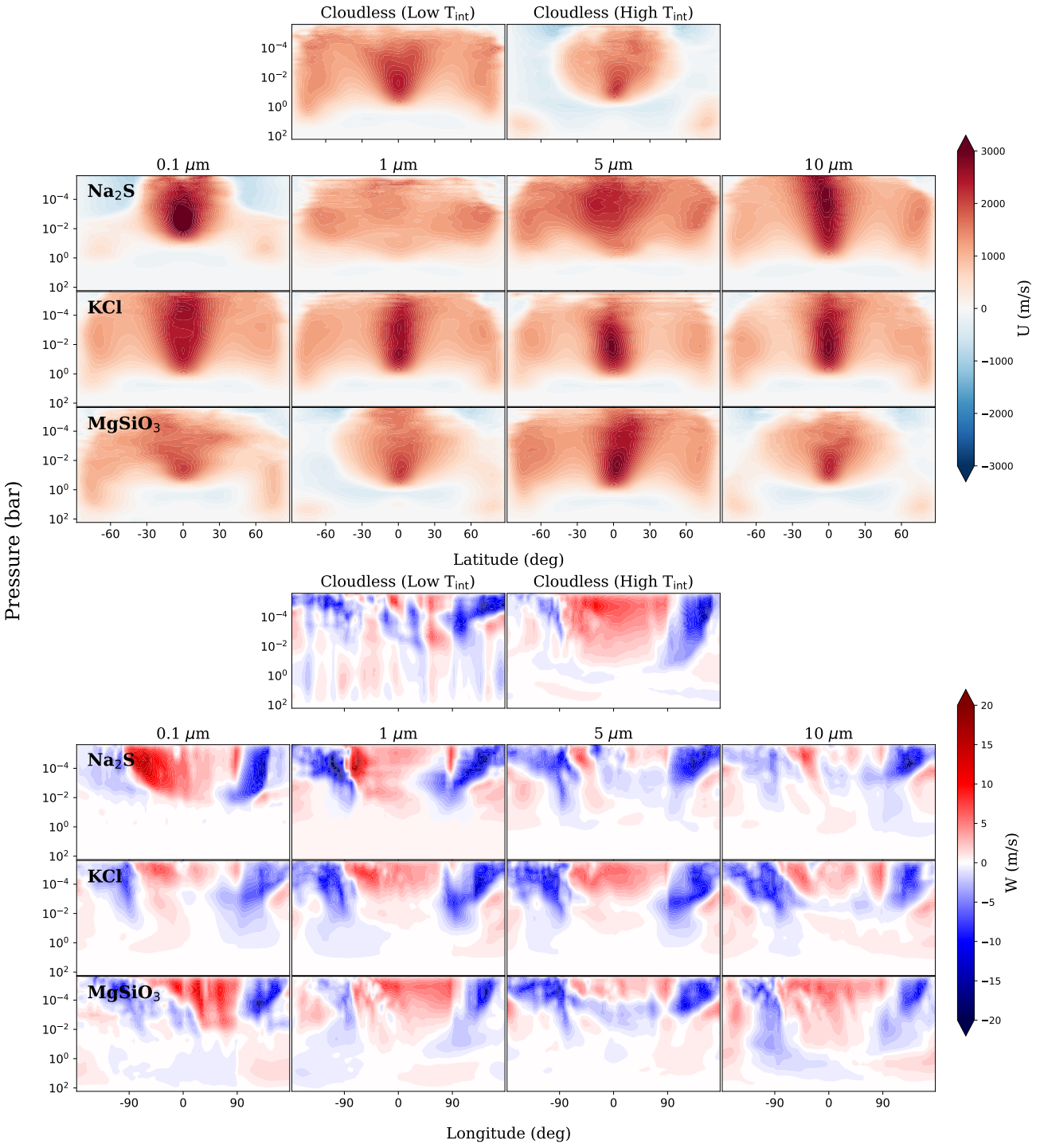

Fig. 3. Top: Zonal-mean zonal wind speed (Latitudinal distribution of Zonal component of wind (U) averaged over longitudes) for all models. Within each subplot, the x-axis shows the latitude and the y-axis the pressure. The first row shows cloudless models, low (100 K) and high (381 K) T_{int}. Rows 2, 3, and 4 correspond to Na_2S, KCl, and $MgSiO_3$ clouds (with High T_{int}), respectively, with each column representing a different particle size indicated at the top. Bottom: Same as Top, but for longitudinal distribution of the Vertical component of wind (W) averaged over latitudes. The vertical component shows the strength of upwelling on the dayside and downwelling on the nightside for different models.

	Na_2S		KCl		$MgSiO_3$	
	Transmission	**Emission**	**Transmission**	**Emission**	**Transmission**	**Emission**
0.1	2.22	12.52	2.52	2.63	2.74	5.60
1	2.25	22.87	2.06	2.12	2.70	1.88
5	2.43	8.72	2.61	2.13	2.81	1.98
10	2.83	1.87	2.81	2.14	2.97	2.54
	Cloudless with low T_{int}				**Cloudless with High T_{int}**	
	2.75	1.97			2.90	2.73

Table 3. χ^2_{red} values calculated for the transmission and emission spectra compared with JWST observations for different cloud species and particle sizes. The rejected models are highlighted in red.

80b. We carried out separate simulations for each cloud species and mean particle size to determine how they individually affect atmospheric dynamics and spectral features.

4.1. Spatial Cloud Distribution

The cloud distribution on the planet is determined by both the thermal structure and the dynamical transport. The subplots of Fig. 4 show the cloud distribution averaged over latitude and longitude. In Fig. A.2, the globally averaged mass mixing ratios of condensate and vapor are compared to the saturation mixing ratio. Comparing the cloud distribution (Fig. 4) with the temperature structure (Fig. 5), it can be seen that the clouds are present in the cooler regions of the planet. In Fig. 4, every row shows a clear trend of cloud distribution with the particle size. Smaller particle-size clouds are lofted high in the atmosphere and are evenly distributed over the planet. As the particle size increases, the clouds settle down to the higher pressures and start forming clusters in the cooler regions of the planet. The clouds are depleted around the super-rotating jet and the dayside. The temperature shapes the cloud boundary in the deep atmosphere, but the winds shape the upper atmosphere.

As seen in Fig. 4, the Na_2S clouds with particle size of 0.1 μm are evenly distributed over the latitude and longitude between the pressures 0.01 bar to 1 bar. At lower pressures, the clouds are depleted near the equator due to a super-rotating jet, along with clouds being evaporated on the dayside. This is observed by the asymmetrical distribution due to the Eastern winds. The distribution of 0.1 μm Na_2S clouds is similar to the distribution of the temperature. The clouds are present in the cooler regions of the planet and are lofted high in the atmosphere. The 1 μm Na_2S clouds are dense at the poles at higher pressure (0.1 - 1 bar) while scarce near the equator, dayside, and lower pressures. The eastern limb is less cloudy than the western limb due to the eastward transport by the equatorial jet. With the larger particle size, the clouds settle down at high pressures and concentrate near the poles. Hence, they are not evenly distributed over the planet, but according to the temperature structure. The cloud distribution of the 5 μm cloud is very uneven. The clouds are clustered near the poles with scarce distribution near the equator, and evenly distributed over the day and nightside. These clouds have settled down to the higher pressures and are only present in the cooler regions of the planet. The GCM with 10 μm Na_2S clouds is depleted throughout the planet. The clouds are mainly distributed near the poles over all the longitudes. Due to the large particle size, even if there are cooler regions at lower pressures, the clouds have settled down to the higher pressures.

We now turn to the KCl clouds. KCl has both a lower abundance and a cooler condensation temperature. However, as for the Na_2S case, they can still evaporate at the low pressures of the dayside. The 0.1 μm KCl clouds are evenly distributed over the latitudes. As the particle size increases, the depletion due to the super-rotating jet increases. The evenly spread clouds start forming clusters with an increase in abundance in the regions where the winds are not so strong (The zonal-mean zonal wind is similar to cloudless GCMs; Fig. 3). As shown in Fig. 4, 0.1 μm KCl clouds are present on the nightside and evaporate from the dayside. A shift can be seen in the longitudinal distribution due to the strong super-rotating jet and the prograde winds. The clouds are distributed over all latitudes. Similar distribution is seen for 1 μm KCl clouds, but the clouds are now settled compared to 0.1 μm KCl clouds. But for 5 and 10 μm KCl clouds are only present near the polar region and hence over all the longitudes. The increase in size from 5 to 10 μm only increases the cluster size at the polar regions. The KCl clouds are formed in the cooler regions of the planet. The smaller particles are lofted high and hence evenly distributed over the planet. The larger particles settle down, deviating from the temperature structure of the planet, and start forming clusters in the atmosphere.

Finally, the last two rows of Fig. 4 show the distribution of $MgSiO_3$ clouds. These clouds have a much higher condensation temperature and, as such, condense in the deep layers of the planet, around 10 bars. Above the 10 bar level, the clouds are mainly affected by dynamical mixing and not much by the thermal structure. As a consequence, small particles, such as 0.1 and 1 μm are lofted up high in the atmosphere and homogeneously cover the planet, whereas clouds formed of 5 or 10 μm particles are confined below the photospheric layers.

4.2. Effect of Clouds on Temperature

Overall, the photospheric temperature structure of the planet is very homogeneous with a very efficient heat redistribution (f=1.04). Adding different clouds to the planet causes changes in the temperature structure depending on the species, particle size, and abundance of the clouds.

The pressure-temperature profile of cloudless GCMs is shown in Fig. 1. Different clouds affect the temperature structure depending on the species, particle size, abundance, and location of the clouds. The condensation curves of the Na_2S, KCl, and $MgSiO_3$ clouds are shown in Fig. 1 along with the pressure-temperature profile of the cloudless GCM. The pressure-temperature profile of the cloudless GCM crosses the condensation curves of Na_2S and KCl clouds, whereas the pressure-temperature profile does not cross the condensation curve of $MgSiO_3$ clouds. As a consequence, for our low T_{int} model, only Na_2S and KCl clouds can be present in the modelled atmosphere. In order to study the possible distribution and impact of $MgSiO_3$ on the spectra, we further simulate models with hotter deep thermal profiles, corresponding to a higher T_{int} of 381 K as proposed by Wiser et al. (2025).

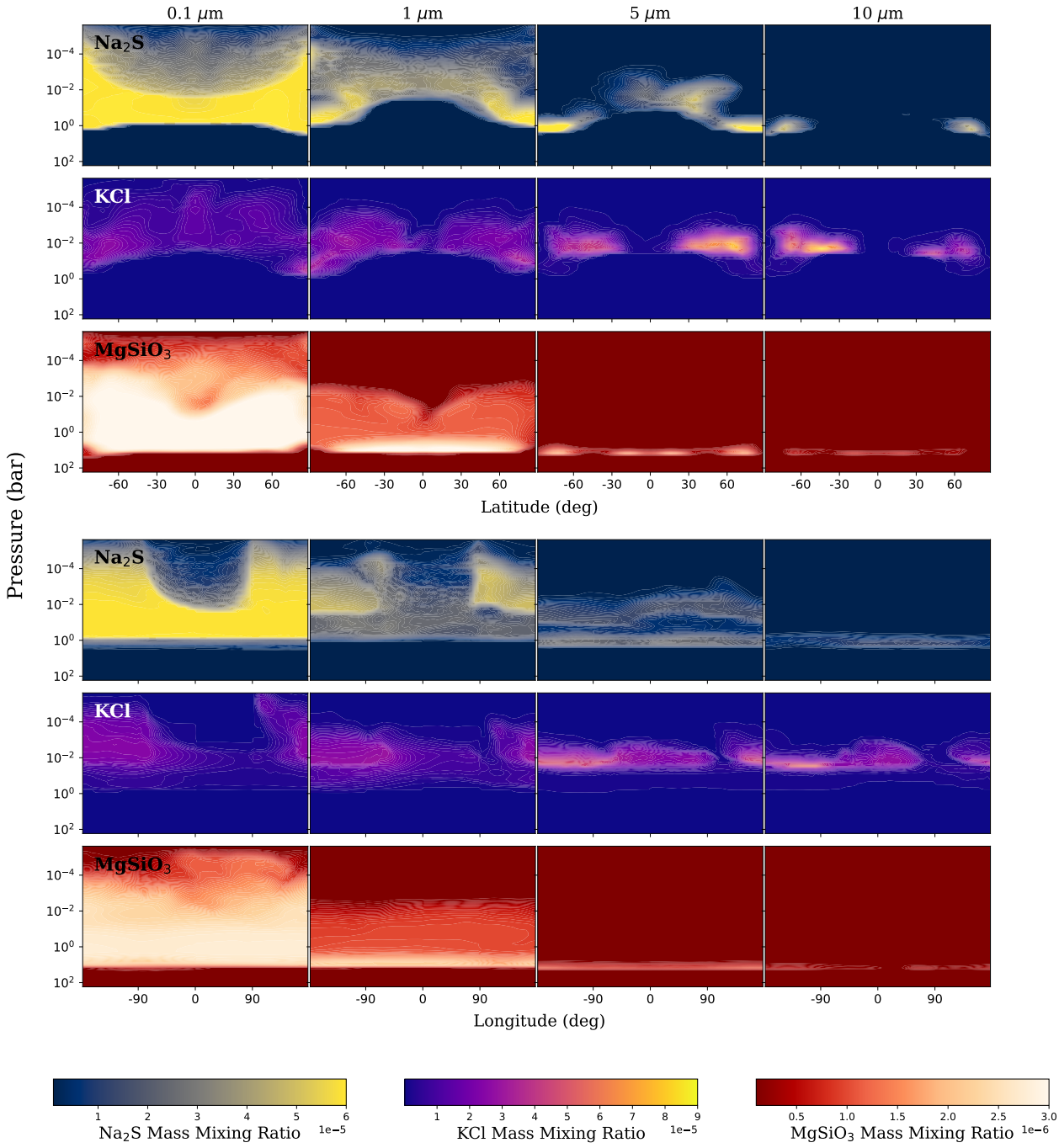

Fig. 4. Top: Latitudinal distribution of clouds (shows equatorial and polar regions), averaged over longitudes for all models. Within each subplot, the x-axis shows the latitude and the y-axis the pressure. Rows 1, 2, and 3 correspond to Na_2S, KCl, and $MgSiO_3$ (with High T_{int}) clouds, respectively, with each column representing a different particle size indicated at the top. Bottom: Same as Top, but for longitudinal distribution of clouds (shows dayside and nightside of the planet), averaged over latitudes for all models.

0.1 μm Na_2S clouds affect the temperature structure of the planet significantly. The 0.1 micron Na_2S clouds have a strong radiative feedback on the atmosphere. This feedback depends on planetary location: on the dayside and eastern terminator, they create a strong thermal inversion at pressure less than 0.02 bar and cool down the layers below it. On the nightside and the western terminate, they lead to a cooler atmosphere. The thermal inversion also occurs on the western terminator, but at a lower

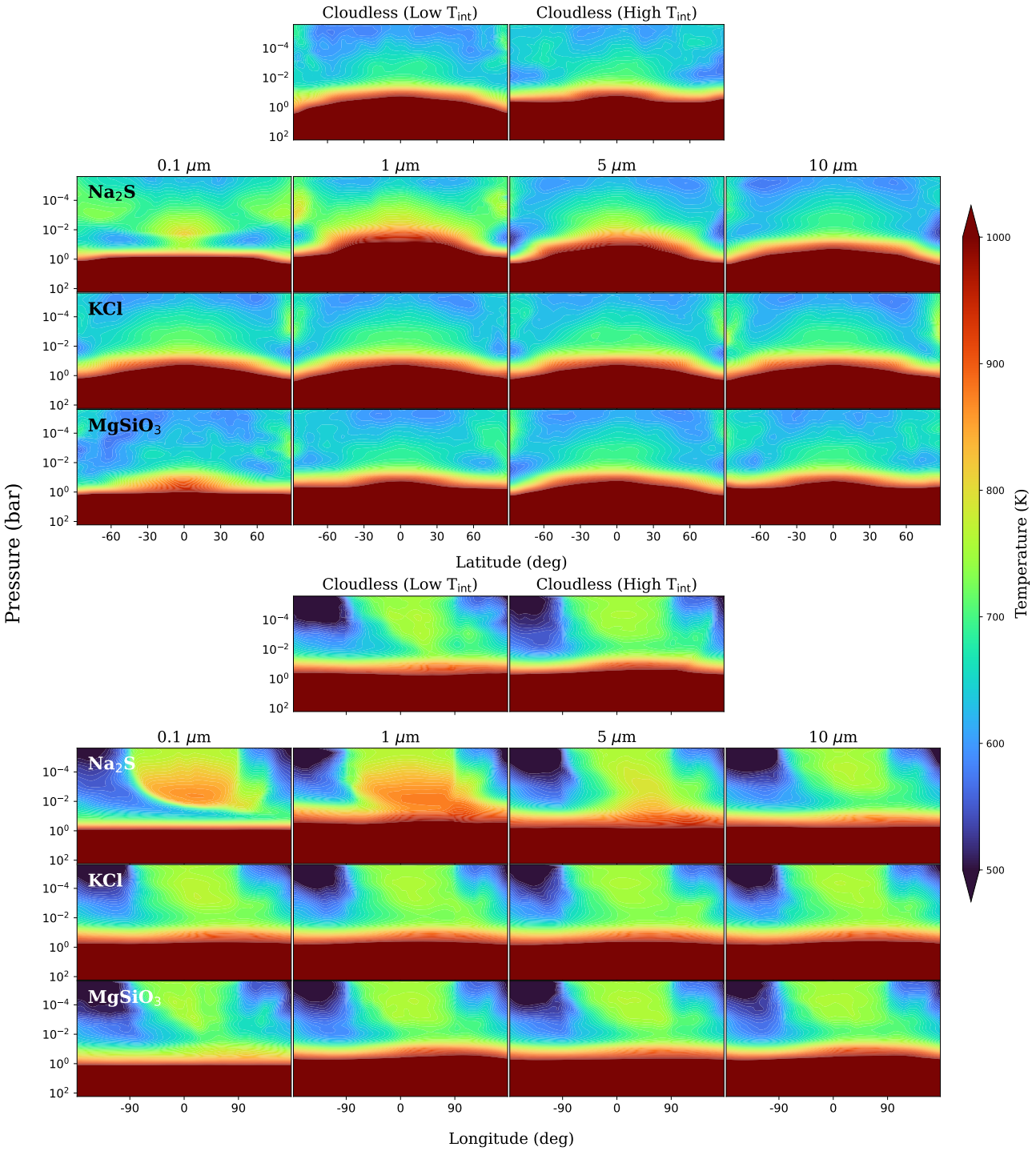

Fig. 5. Top: Latitudinal distribution of temperature (shows equatorial and polar regions), averaged over longitudes for all models. Within each subplot, the x-axis shows the latitude and the y-axis the pressure. The first row shows cloudless models, low (100 K) and high (381 K) T_{int}. Rows 2, 3, and 4 correspond to Na_2S, KCl, and $MgSiO_3$ (with High T_{int}) clouds, respectively, with each column representing a different particle size indicated at the top. Bottom: Same as Top, but for longitudinal distribution of clouds (shows dayside and nightside of the planet), averaged over latitudes for all models.

pressure of 0.001 bar. Due to the high Mass Mixing Ratio, the 0.1 μm Na_2S particles are very efficient in absorbing the stellar radiation, causing the temperature inversion above the clouds. They shield the atmosphere below them from the stellar radiation and hence cool the atmosphere below them. The inversion is stronger on the dayside as the stellar radiation is more intense on the dayside. The nightside is cooler because the dayside is cooler at pressures greater than 0.02 bars. So less heat is transported to the nightside. 1 μm Na_2S clouds absorb across the spectrum, leading to strong heating in the location of the clouds. Hence, a heating effect is seen in the upper atmosphere (above 1 bar) where the clouds are present. There is no cooling effect as these clouds do not absorb the stellar radiation as efficiently as the 0.1 μm Na_2S clouds. The 5 μm Na_2S clouds do not absorb radiation efficiently and hence do not affect the temperature structure of the planet significantly; they slightly increase the temperature in the upper atmosphere. The 10 μm Na_2S clouds mostly follow the temperature structure of the cloudless GCM due to lower abundance and not significant absorption of radiation.

KCl clouds being optically thin, these clouds do not affect the temperature structure of the planet significantly. From Fig. 1, we see that the condensation curve that was crossing the cloudless dayside average pressure-temperature profile between 0.002 to 0.05 bar. When KCl clouds are included, they raise the temperature in this region. As a result, the dayside average pressure-temperature profile no longer crosses the condensation curve, meaning that KCl is unlikely to condense there. However, the condensation curve still intersects the pressure-temperature profiles from other regions of the planet, where cloud formation may still occur. These clouds are present in the cooler regions of the planet and absorb radiation efficiently, hence slightly cooling the atmosphere below them while heating the upper atmosphere. The change in the temperature structure is not significant.

With the high T_{int}, the pressure-temperature profile crosses the condensation curve of $MgSiO_3$ clouds. The 0.1 μm $MgSiO_3$ clouds are present all over the planet. With a small particle size, these clouds are lofted high in the atmosphere. These clouds have very high albedo, reflecting the stellar light to space and hence cooling the atmosphere below them. 1, 5, and 10 μm $MgSiO_3$ clouds are present deep in the atmosphere and do not affect the temperature structure of the planet. As explained in Section 2.6, our $MgSiO_3$ clouds were implemented in the GCM with a 1000 times reduced opacity. As a consequence, the radiative effect of the clouds seen in our models is a lower bound of what would be expected in the real planet.

4.3. Effect of Clouds on Dynamics

Clouds alter the thermal distribution, which in turn alters atmospheric dynamics and transport across the atmosphere by influencing the heating and cooling characteristics of the atmosphere.

Different cloud species affect the wind structure differently. This can be seen in Fig. 3. The zonal, meridional, and vertical components, means over latitude and longitude, are shown in Appendix Fig. A.3, A.4, and A.5, respectively. As seen in Fig. 3, the 0.1 μm Na_2S cloud case, when compared to the cloudless scenario, exhibits a zonal-mean wind structure characterized by a strong equatorial jet and retrograde winds at high latitudes. Similar features are observed in the 1 μm and 10 μm $MgSiO_3$ cloud cases, which were both modelled with a high T_{int}. Interestingly, these dynamical patterns closely resemble those seen in the cloudless high-T_{int} model, suggesting that 0.1 μm Na_2S clouds had much more effect on the dynamics, and 1 and 10 μm $MgSiO_3$ had almost no impact on the dynamics. The strong impact of 0.1 μm Na_2S can be attributed to the presence of a temperature inversion. The increase in temperature with altitude above 0.1 bar can develop a pronounced upwelling region on the dayside. This vertical motion could modify angular momentum transport, ultimately leading to the observed polar flow reversal similar to the High-T_{int} cloudless case. On the other hand, we see that 0.1 and 5 μm $MgSiO_3$ clouds have a strong effect on the dynamics. Even though $MgSiO_3$ clouds are modelled with High T_{int}, the dynamics showcased by 0.1 and 5 μm $MgSiO_3$ clouds are similar to the cloudless low-T_{int} case. Also, it is interesting that the presence of 1 μm Na_2S clouds significantly weakens, or nearly eliminates, the equatorial jet. Rest of the cases, the atmospheric flow is similar to the cloudless case; the strength varies depending on the cloud species. In Appendix Fig. A.6, we show how the jet speed (maximum zonal-mean zonal wind) varies with cloud particle size for the 3 cloud species.

Fig. 6 presents the meridional wind component multiplied by the sign of latitude, effectively illustrating the direction of atmospheric flow with respect to the equator. This projection highlights regions of poleward and equatorward transport. From Fig. 6, we can see that the winds and their direction have similar distribution over longitude, but the depth of these winds that move towards the equator or poles and their strength differ with different cloud cases. Fig. 7 shows the K_{zz} for all GCM cases. The K_{zz} profiles for different cloud cases are calculated by $K_{zz}(p) \sim H.w_{\rm rms}(p)$, where H is the scale height and w is the vertical component of winds as a function of pressure (Lewis et al. 2010; Moses et al. 2011). Although this approach usually overestimates the mixing strength by one or two orders of magnitude (Parmentier et al. 2013), it is useful in our case to compare the relative mixing efficiency of the different models. We see that all models have approximately the same mixing strength at pressures lower than 0.1 bar. However, the presence of clouds tends to reduce the mixing strength in the deep layers of the atmosphere, with some cloud species, such as Na_2S and KCl, reducing the mixing by 2 orders of magnitude.

4.4. Comparison with the Observations

The transmission and emission spectra were obtained for cloudy GCMs with different particle sizes of Na_2S, KCl, and $MgSiO_3$ clouds. The transmission and emission spectra were compared with the observations from JWST. The transmission and emission spectra are shown in Fig. 8. The nightside temperature-pressure profiles and emission spectra are shown in Appendix Fig. A.7.

Condensation clouds have been shown to exist on numerous planets, and we expect them to form in WASP-80b. Particularly, as shown in Fig. 1, the thermal profile of the planet crosses the condensation curves of Na_2S, KCl near the photosphere and, for the high T_{int} scenarios, the condensation curve of $MgSiO_3$ at depth. As a consequence, even though both transmission and emission spectra are compatible with the cloudless model, we do expect clouds to form in this atmosphere. The WASP-80b dataset, therefore, provides us with an opportunity to determine which kind of clouds can form and which ones are unlikely to form. For this, we run models with three different types of clouds, and, for each of them, 4 different mean particle sizes. Each of these clouds can have an indirect effect on the spectra by changing the thermal structure of the planet and a direct effect by spectral signatures in the emission and transmission spectra.

10 μm Na_2S clouds provide a good match for the emission and transmission, with a caveat that the CH_4 is over-predicted and CO_2 is under-predicted in transmission. As seen in Fig. 4

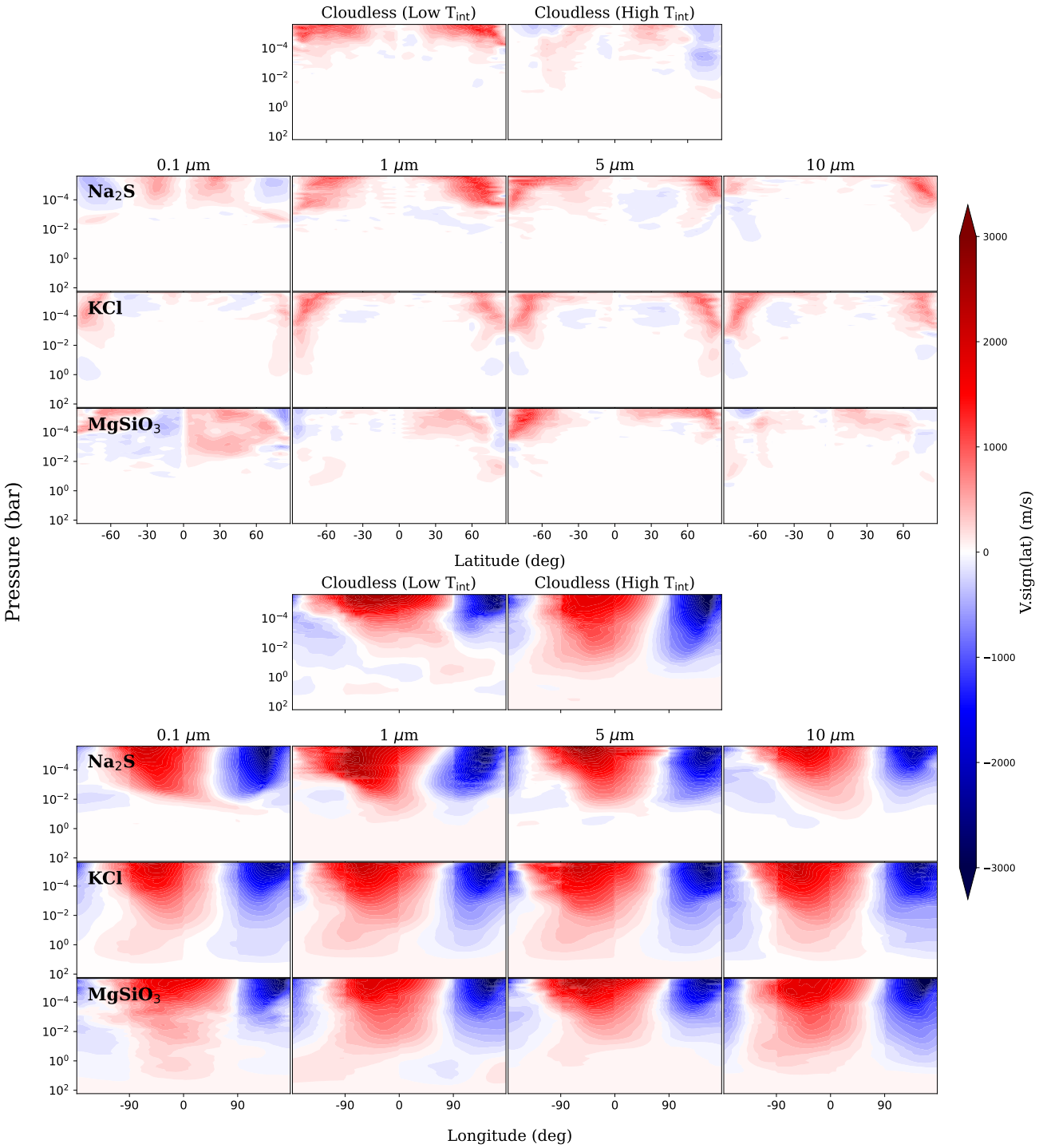

Fig. 6. Same as Fig. 4 but for meridional wind multiplied by the sign of latitude to indicate wind towards (negative) or away (positive) from the equator.

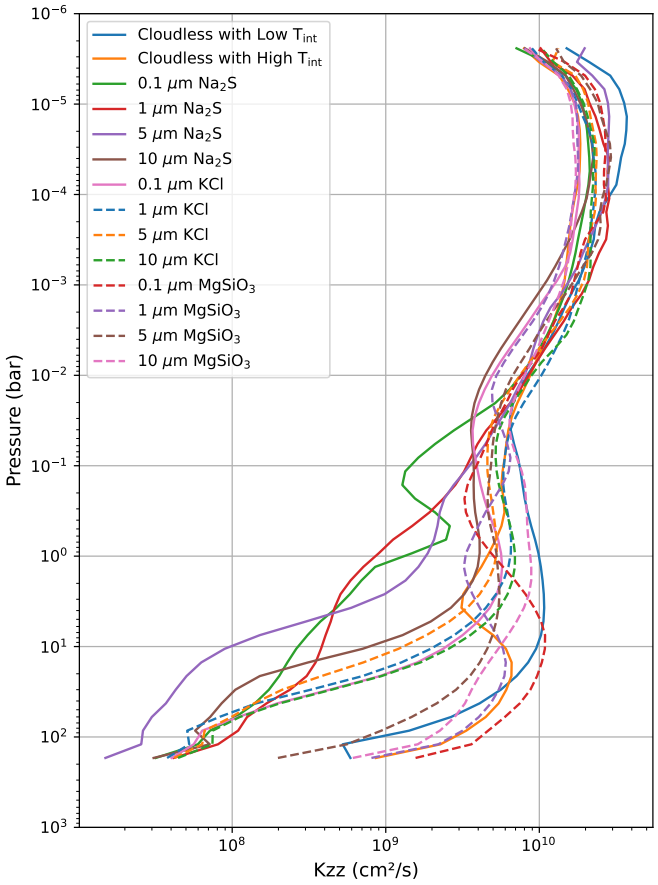

Fig. 7. K_{zz} profiles for different cloud cases. K_{zz} was calculated as the root mean square of the vertical velocity times the vertical scale height.

and discussed in Section 4.1, 10 μm Na_2S clouds tend to concentrate at pressures of 0.1 bar and near the poles, making them both invisible to the spectra and having a weak impact on the radiative transfer. Whereas, the models with 0.1, 1, and 5 μm Na_2S clouds are all ruled out by the data; this is mainly due to their effect on the dayside thermal profile. Indeed, the presence of 0.1 μm clouds leads to a strong thermal inversion on the dayside atmosphere, leading to emission features rather than absorption, which is incompatible with the observations. For the 1 and 5 μm cases, the dayside thermal profile is not inverted; however, the greenhouse effect of the clouds on the nightside atmosphere leads to a hotter and more isothermal dayside. Thus, despite the lack of strong cloud coverage on the dayside, the emission spectrum becomes too large and the spectral features too small to be compatible with the observations.

For the transmission spectra, the 0.1, 5, and 10 μm Na_2S clouds can fit the data. The 0.1 μm Na_2S clouds can fit the terminator data. These clouds lift the baseline of the transmission spectrum at lower wavelength regions (<2.5 μm) where the data is unavailable (NIRISS/SOSS: This observation will be part of the JWST-GO-5924 program; PI: David Sing; NIRCam F210M: The data was not utilized due to excess noise). 5 μm Na_2S clouds also lift the baseline of the transmission spectrum at lower wavelength regions, but not as much as the 0.1 μm Na_2S clouds. This is due to the distribution of clouds, where the smaller particles are present in the upper atmosphere, leading to a higher baseline. As the size increases, the changes in the baseline decrease. The 10 μm Na_2S clouds are present in the deep atmosphere and do not affect the transmission spectrum. On the other hand, the 1 μm Na_2S clouds suppress all the features in the transmission spectrum and fail to reproduce the CO_2 feature at 4.3 μm. This is because these clouds are present in the upper atmosphere, affecting the baseline of the transmission spectrum. Although the spatial distribution of 0.1 and 1 μm Na_2S clouds is similar at lower pressures, the 0.1 μm particles provide a better fit to the observations. This is because their absorption cross-section is higher at shorter wavelengths, allowing spectral features at longer wavelengths to be unaffected. In contrast, the 1 μm particles exhibit significant absorption across the entire wavelength range, resulting in a broad suppression of spectral features and a poorer match with the data.

For KCl clouds, all the models with different particle sizes can fit the dayside emission spectrum and the terminator observations. KCl clouds do not affect the emission spectrum significantly since they do not affect the temperature structure of the planet significantly due to their low optical depth (Fortney 2005; Lee & Ohno 2025). KCl clouds affect the spectrum at wavelengths below 2.5 μm by raising the baseline of the transmission spectrum, with the magnitude of this effect depending on particle size. As the particle size increases, the clouds settle down to the higher pressures, and the transmission spectrum is less affected by the clouds. The baseline of the transmission spectrum is elevated at lower wavelengths, primarily by 0.1 μm KCl clouds, and it is unaffected by the 10 μm KCl clouds.

The limited $MgSiO_3$ clouds (resulting in reduced opacity) were included in the GCMs with high T_{int}. As seen in Fig. 8, the 1 μm $MgSiO_3$ clouds have the best fit to observations according to Table 3. The 1 μm $MgSiO_3$ clouds lower the flux at higher wavelengths around 10 μm, which leads to a better fit to the dayside emission spectrum. These clouds reflect stellar radiation efficiently, resulting in the cooling of the atmosphere below them. This also leads to a high planetary albedo. The 5 and 10 μm $MgSiO_3$ clouds do not affect the dayside emission spectrum significantly due to low abundance and reduced opacity. On the other hand, 0.1 μm $MgSiO_3$ clouds underestimate the dayside emission spectrum as they lower the dayside temperature of the planet. The 0.1 μm $MgSiO_3$ clouds are present throughout the atmosphere and even at low pressures. With the high reflectivity of these clouds, the stellar radiation is reflected to space, and hence the dayside temperature is lower than the cloudless case. Even for the transmission spectrum, all the models with $MgSiO_3$ clouds can fit the terminator observations. The 0.1 μm $MgSiO_3$ clouds lift the baseline of the transmission spectrum in the lower wavelength region but do not affect the rest of the spectrum significantly. A spectral feature is seen at 10 μm, which is due to the absorption of the clouds.

For each GCM scenario, we generated the emission and transmission spectra and compared them against the observations, which enabled us to place stronger constraints on the cloud properties of the planet. The χ^2_{red} was calculated for each model comparing the transmission and emission spectra with the observations. The chi-square was used to rule out the models that are not able to fit the observations. According to the Emission models from Table 3, we see that smaller particle size Na_2S or $MgSiO_3$ clouds have a much higher χ^2_{red} value than other models. Remaining models have comparable χ^2_{red} values, making it difficult to choose one correct model, but we can say with certainty that the clouds rejected by these models (smaller particle size Na_2S or $MgSiO_3$ clouds) should not be present on the planet. On the other hand, all the transmission models have similar χ^2_{red}. We cannot reject any model just based on the transmission spectrum; whereas the transmission spectrum is usually thought to be most sensitive to clouds (Fortney 2005; Inglis et al. 2024; Welbanks

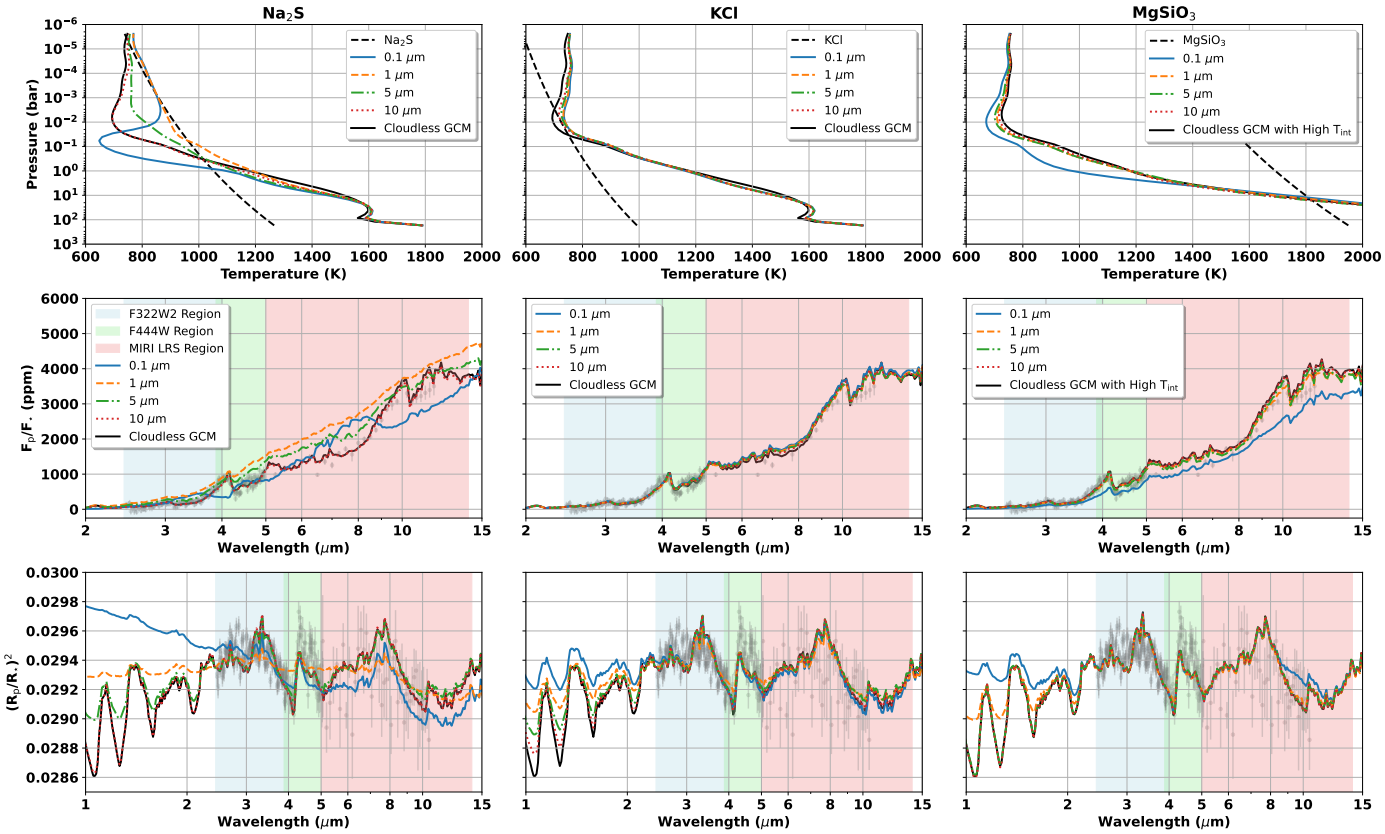

Fig. 8. Top Row: Dayside averaged Pressure-Temperature profiles for different particle sizes along with the cloudless case (solid black line). The condensation curve for the corresponding cloud species is plotted with a black line. Middle Row: Emission Spectra from GCM models along with the cloudless case (solid black line) and JWST observation (grey). Bottom Row: Transmission Spectra from GCM models along with the cloudless case (solid black line) and JWST observation (grey).

et al. 2024), we find the opposite for our models of WASP-80b. Overall, these results demonstrate that a combined analysis of transmission and emission spectra is required to robustly characterize clouds on warm Jupiters, as interpretations based on a single spectrum may be misleading.

5. Discussions and Conclusion

We modelled the three-dimensional atmospheric structure of the warm Jupiter WASP-80b, both with and without clouds, and compared the results to JWST emission and transmission spectra. Our model suite included cloud-free cases with low and high internal heat flux (T_{int}), as well as cloudy cases with various mean particle radii (0.1, 1, 5, and 10 μm) and different condensate species (Na_2S, KCl, and $MgSiO_3$), treated as radiatively active tracers. This grid of models allowed us to investigate how the thermal structure and atmospheric dynamics respond to different cloud properties and internal heat flux scenarios.

The spatial distribution of clouds depends on the local pressure, local temperature, dynamics, and the condensation properties of individual species. We observe the similarity between the cloud distribution (Fig. 4) and the temperature distribution (Fig. 5). The dynamics of the planet are an additional factor that comes into play. In addition, dynamics play a key role: the balance between vertical winds and particle settling velocities sets the vertical extent of the cloud deck, while horizontal winds shape the global distribution, producing asymmetries between the planetary limbs. Such limb asymmetries have already been detected in JWST observations of several exoplanets (Espinoza et al. 2024; Murphy et al. 2024; Mukherjee et al. 2025). Moreover, radiative feedback from clouds amplifies temperature contrasts between the limbs, as demonstrated by Murphy et al. (2025) using the same GCM framework.

Every cloud species and particle size has different optical properties and optical depth, which in turn determines the strength of their radiative feedback. Na_2S and $MgSiO_3$ clouds generally have a strong feedback, while KCl clouds, being optically thin, have a weak radiative feedback. The radiative feedback also depends on the abundance of the clouds and their spatial distribution. Cloud coverage on the dayside in particular can significantly alter the atmospheric dynamics. The 0.1 μm Na_2S, 0.1 μm $MgSiO_3$, 5 μm $MgSiO_3$ clouds had a major impact on the zonal-mean zonal wind structure, whereas the other cloud cases resulted in wind patterns similar to their respective cloud-free simulations with low or high tint. The changes in the wind structure are due to the radiative feedback of the different cloud cases. The effect of radiative feedback on dynamics can be further seen in the vertical and meridional wind components (and consequently in the K_{zz} profiles; see Figs. A.5 and A.4). This shows the importance of radiative feedback of clouds on the dynamics of warm giant planets, especially when the clouds are present on the dayside. In atmospheres with highly efficient heat redistribution ($f = 1.04$), even small perturbations to the thermal structure can drive noticeable dynamical changes. In addition to clouds, the effective internal temperature also strongly modulates atmospheric dynamics, consistent with Komacek et al. (2022).

As shown in Section 3.1, our cloud-free model exhibits very good agreement with both the emission and transmission spectra

of WASP-80b, without requiring any additional tuning beyond adopting the chemical abundances retrieved from the 1D spectral analysis and setting the reference pressure in post-processing. This result demonstrates that global circulation models (GCMs) are capable of capturing most of the physics governing the three-dimensional thermal structure of this warm giant planet, thereby providing a robust benchmark for GCM studies. The good agreement with observations is surprising, as the temperature profile of WASP-80b crosses multiple condensation curves.

Models including KCl clouds also reproduce the observations with high accuracy. There are several reasons: (i) the KCl condensation curve only marginally intersects the dayside temperature–pressure profile (see Fig. 8), with the majority of cloud formation occurring on the nightside (see Fig. A.7); (ii) the elemental abundances of K and Cl are relatively low; and (iii) KCl clouds are optically thin. As a result, their impact on the dayside emission spectrum is negligible and only minor in the transmission spectrum. Together, these effects cause the spectra of KCl-cloud models to closely resemble those of the cloud-free case, even when clouds are present.

Models with large cloud particle sizes are able to reproduce the spectra. In these cases, efficient gravitational settling removes clouds from the observable atmosphere, minimizing their spectral impact. Powell & Zhang (2024) have shown that cloud particle distributions can extend up to 100 μm; however, particles larger than ~10 μm may not significantly affect the spectra. A caveat remains that the role of deep-interior convergence is not considered here (see Section 2.8).

From this study, we were able to rule out certain cloud species that are not consistent with the JWST observations. 0.1 μm Na_2S clouds are optically thick and cause a strong radiative feedback, leading to a temperature inversion. Larger Na_2S particles (1 and 5 μm) instead raise the photospheric temperature, resulting in an overestimation of the emitted flux and the emission spectrum. Indeed, it remains debated whether Na_2S clouds can form in exoplanet atmospheres, as their high surface energies create a substantial barrier to nucleation (Gao et al. 2020).

In this work, we limited the formation of $MgSiO_3$ clouds (see Section 4), although their condensation curve is consistent with the 3× Solar case. One possible approach to overcome this instability is to gradually increase the condensate abundance once the atmosphere becomes stable (Roman et al. 2021), which would allow $MgSiO_3$ clouds to form without additional constraints. This will be explored in future studies of this planet.

Finally, we note that certain clouds (e.g., 0.1 μm Na_2S) can reproduce the dayside observations but cannot match the terminator spectra. This demonstrates the importance of multi-view observations in constraining exoplanet atmospheres, as dayside and limb spectra provide different, complementary information.

From our analysis, we draw the following main conclusions:

1. WASP-80b is a warm Jupiter with a very efficient heat redistribution. The thermal distribution of the planet is very homogeneous, with the possibility that the planet may be cloudless.
2. The cloudless GCM was able to reproduce the observations of the planet with a good fit to the dayside and terminator observations. The relatively low abundance of CH_4 on the terminator can be due to photochemistry or due to quenching resulting from the high interior temperature of the planet.
3. Large particle clouds of any species can be present as they settle down in the atmosphere and do not affect the spectra significantly.
4. KCl clouds can be present on the planet as they do not cause a significant change in transmission or emission spectrum for this planet.
5. Small Na_2S particle clouds of sizes 0.1, 1, 5 μm along with 0.1 μm $MgSiO_3$ are inconsistent with the JWST observations.

Overall, we show that multiple cloudy scenarios are compatible with the apparently cloudless spectrum of WASP-80b. We demonstrate that observations at short wavelengths should break the degeneracy between these scenarios and determine whether WASP-80b is truly cloudless or whether clouds exist but are not currently affecting the observations.

The possibility of the presence of PH_3 and CS_2 in the atmosphere of WASP-80b is out of scope for this study, but the chemistry for these molecules should be further explored. A recent study (Veillet et al. 2025) showed that there is an increase in the production of CS_2 on a planet with a temperature of around 800 K with an updated chemical network. A detailed study on the presence of PH_3 and CS_2 on WASP-80b should be explored in detail.

We can enhance this framework and impose tighter constraints on cloud properties by incorporating more realistic assumptions from cloud microphysics, particularly regarding cloud species and particle sizes. A dedicated microphysical study—similar to that of Powell & Zhang (2024), focused on atmospheres with equilibrium temperatures around 800 K, could inform better assumptions for particle size distributions, especially since different condensates have been shown to produce distinct particle sizes. We can also increase the complexity by including multiple cloud species simultaneously. This would lead to complex effects on the thermal structure.

WASP-69b (T_{eq} ~ 963 K), WASP-80b (T_{eq} ~ 820 K), and WASP-107b (T_{eq} ~ 735 K) are planets of similar size, orbiting stars of the similar spectral type, and lie within the same equilibrium temperature range. Yet, their atmospheres exhibit different characteristics. WASP-69b and WASP-80b show clear differences in heat redistribution efficiency, and clouds are favored in models to fit the JWST spectrum of WASP-69b, either through high albedo or by creating a highly inhomogeneous dayside (Schlawin et al. 2024). In contrast, WASP-80b shows no strong observational indications of clouds in its atmosphere. On the other hand, the JWST transmission spectrum of WASP-107b strongly supports the presence of a cloud deck (Welbanks et al. 2024; Sing et al. 2024) as well as strong limb asymmetry (Murphy et al. 2025). A detailed comparative study of these planets, within this shared temperature regime, using general circulation models (GCMs) coupled with clouds, is necessary to understand the origins of their atmospheric diversity better (Mehta et al., in preparation).

Acknowledgements. This work was supported by the French government through the France 2030 investment plan managed by the National Research Agency (ANR), as part of the Initiative of Excellence Université Côte d'Azur under reference number ANR-15-IDEX-01. The authors are grateful to the Université Côte d'Azur's Center for High-Performance Computing (OPAL infrastructure) for providing resources and support.

References

Adcroft, A., Campin, J.-M., Hill, C., & Marshall, J. 2004, Monthly Weather Review, 132, 2845
Amundsen, D. S., Tremblin, P., Manners, J., Baraffe, I., & Mayne, N. J. 2017, Astronomy and Astrophysics, 598, A97
Batalha, N. & Marley, M. 2020, Refractive Indices For Virga Exoplanet Cloud Model

Batygin, K. & Stevenson, D. J. 2010, ApJ, 714, L238
Bell, T. J., Welbanks, L., Schlawin, E., et al. 2023, Nature, 623, 709
Carone, L., Baeyens, R., Mollière, P., et al. 2020, Monthly Notices of the Royal Astronomical Society, 496, 3582
Charnay, B., Meadows, V., Misra, A., Leconte, J., & Arney, G. 2015, The Astrophysical Journal, 813, L1
Collins, W. D., Rasch, P. J., Boville, B. A., et al. 2004, NCAR Tech. Note NCAR/TN-464+ STR, 226, 1326
Drummond, B., Hébrard, E., Mayne, N. J., et al. 2020, 636, A68
Espinoza, N., Steinrueck, M. E., Kirk, J., et al. 2024, Nature, 632, 1017
Feng, Y. K., Line, M. R., Fortney, J. J., et al. 2016, The Astrophysical Journal, 829, 52
Fortney, J. J. 2005, Monthly Notices of the Royal Astronomical Society, 364, 649
Fortney, J. J., Dawson, R. I., & Komacek, T. D. 2021, Journal of Geophysical Research (Planets), 126, e06629
Fortney, J. J., Lupu, R. E., Morley, C. V., Freedman, R. S., & Hood, C. 2019, The Astrophysical Journal Letters, 880, L16
Fortney, J. J., Marley, M. S., & Barnes, J. W. 2007, The Astrophysical Journal, 659, 1661
Freedman, R. S., Lustig-Yaeger, J., Fortney, J. J., et al. 2014, ApJS, 214, 25
Fu, G., Mukherjee, S., Stevenson, K. B., et al. 2025, ApJ, 989, L17
Gao, P., Thorngren, D. P., Lee, E. K. H., et al. 2020, Nature Astronomy, 4, 951
Gharib-Nezhad, E. S., Batalha, N. E., Chubb, K., et al. 2024, RAS Techniques and Instruments, 3, 44
Guillot, T., Burrows, A., Hubbard, W. B., Lunine, J. I., & Saumon, D. 1996, ApJ, 459, L35
Guillot, T., Fletcher, L. N., Helled, R., et al. 2023, in Astronomical Society of the Pacific Conference Series, Vol. 534, Protostars and Planets VII, ed. S. Inutsuka, Y. Aikawa, T. Muto, K. Tomida, & M. Tamura, 947
Guillot, T. & Showman, A. P. 2002, A&A, 385, 156
Inglis, J., Batalha, N. E., Lewis, N. K., et al. 2024, The Astrophysical Journal Letters, 973, L41
Iyer, A. R., Line, M. R., Muirhead, P. S., Fortney, J. J., & Gharib-Nezhad, E. 2023, The Astrophysical Journal, 944, 41
Jacobs, B., Désert, J.-M., Gao, P., et al. 2023, The Astrophysical Journal Letters, 956, L43
Kataria, T., Showman, A. P., Fortney, J. J., Marley, M. S., & Freedman, R. S. 2014, The Astrophysical Journal, 785, 92
Kataria, T., Showman, A. P., Fortney, J. J., et al. 2015, The Astrophysical Journal, 801, 86
Kataria, T., Showman, A. P., Lewis, N. K., et al. 2013, The Astrophysical Journal, 767, 76
Kataria, T., Sing, D. K., Lewis, N. K., et al. 2016, The Astrophysical Journal, 821, 9
Khachai, H., Khenata, R., Bouhemadou, A., et al. 2009, Journal of Physics Condensed Matter, 21, 095404
Komacek, T. D., Gao, P., Thorngren, D. P., May, E. M., & Tan, X. 2022, The Astrophysical Journal Letters, 941, L40
Lacis, A. A. & Oinas, V. 1991, \jgr, 96, 9027
Leconte, J. 2021, Astronomy and Astrophysics, 645, A20
Lee, E. K. H. & Ohno, K. 2025, Astronomy and Astrophysics, 695, A111
Lee, E. K. H., Tsai, S.-M., Hammond, M., & Tan, X. 2023, Astronomy and Astrophysics, 672, A110
Lee, E. K. H., Wardenier, J. P., Prinoth, B., et al. 2022, The Astrophysical Journal, 929, 180
Lewis, N. K., Parmentier, V., Kataria, T., et al. 2017, arXiv e-prints, arXiv:1706.00466
Lewis, N. K., Showman, A. P., Fortney, J. J., Knutson, H. A., & Marley, M. S. 2014, The Astrophysical Journal, 795, 150
Lewis, N. K., Showman, A. P., Fortney, J. J., et al. 2010, 720, 344
Line, M. R. & Parmentier, V. 2016, The Astrophysical Journal, 820, 78
Lines, S., Mayne, N. J., Manners, J., et al. 2019, Monthly Notices of the Royal Astronomical Society, 488, 1332
Liu, B. & Showman, A. P. 2013, The Astrophysical Journal, 770, 42
Lupu, R., Freedman, R., Gharib-Nezhad, E., Visscher, C., & Molliere, P. 2021, Correlated k Coefficients for H2-He Atmospheres; 11 Spectral Windows and 1460 Pressure-Temperature Points
Marley, M. S. & McKay, C. P. 1999, ıcarus, 138, 268
Marley, M. S., Saumon, D., Visscher, C., et al. 2021, The Astrophysical Journal, 920, 85
Mayne, N. J., Debras, F., Baraffe, I., et al. 2017, Astronomy and Astrophysics, 604, A79
Mendonça, J. M. 2020, Monthly Notices of the Royal Astronomical Society, 491, 1456
Mendonça, J. M., Tsai, S.-m., Malik, M., Grimm, S. L., & Heng, K. 2018, The Astrophysical Journal, 869, 107
Montaner, A., Galtier, M., Benoit, C., & Bill, H. 1979, Physica Status Solidi Applied Research, 52, 597
Morel, K., Coulombe, L.-P., Rowe, J. F., et al. 2025, The Astronomical Journal, 169, 277
Morley, C. V., Fortney, J. J., Marley, M. S., et al. 2012, The Astrophysical Journal, 756, 172
Moses, J. I., Visscher, C., Fortney, J. J., et al. 2011, The Astrophysical Journal, 737, 15
Mukherjee, S., Fortney, J. J., Morley, C. V., et al. 2024, The Astrophysical Journal, 963, 73
Mukherjee, S., Fortney, J. J., Wogan, N. F., Sing, D. K., & Ohno, K. 2025, The Astrophysical Journal, 985, 209
Murphy, M. M., Beatty, T. G., Schlawin, E., et al. 2024, Nature Astronomy, 8, 1562
Murphy, M. M., Beatty, T. G., Schlawin, E., et al. 2025, The Astronomical Journal, 170, 61
Parmentier, V., Fortney, J. J., Showman, A. P., Morley, C., & Marley, M. S. 2016, The Astrophysical Journal, 828, 22
Parmentier, V. & Guillot, T. 2014, Astronomy and Astrophysics, 562, A133
Parmentier, V., Guillot, T., Fortney, J., & Marley, M. 2013, in European Planetary Science Congress, EPSC2013–351
Parmentier, V., Guillot, T., Fortney, J. J., & Marley, M. S. 2015, Astronomy and Astrophysics, 574, A35
Parmentier, V., Line, M. R., Bean, J. L., et al. 2018, Astronomy and Astrophysics, 617, A110
Parmentier, V., Showman, A. P., & Fortney, J. J. 2021, Monthly Notices of the Royal Astronomical Society, 501, 78
Powell, D. & Zhang, X. 2024, The Astrophysical Journal, 969, 5
Querry, M. R. 1987, in Conference on Optical Properties of Minerals
Roman, M. & Rauscher, E. 2017, The Astrophysical Journal, 850, 17
Roman, M. & Rauscher, E. 2019, The Astrophysical Journal, 872, 1
Roman, M. T., Kempton, E. M.-R., Rauscher, E., et al. 2021, The Astrophysical Journal, 908, 101
Roth, A., Parmentier, V., & Hammond, M. 2024, Monthly Notices of the Royal Astronomical Society, 531, 1056
Sainsbury-Martinez, F., Wang, P., Fromang, S., et al. 2019, Astronomy and Astrophysics, 632, A114
Schlawin, E., Mukherjee, S., Ohno, K., et al. 2024, The Astrophysical Journal, 168, 104
Schneider, A. D., Carone, L., Decin, L., et al. 2022, Astronomy and Astrophysics, 664, A56
Scott, A. & Duley, W. W. 1996, ApJS, 105, 401
Showman, A. P., Fortney, J. J., Lian, Y., et al. 2009, The Astrophysical Journal, 699, 564
Showman, A. P., Lewis, N. K., & Fortney, J. J. 2015, The Astrophysical Journal, 801, 95
Showman, A. P. & Polvani, L. M. 2011, The Astrophysical Journal, 738, 71
Showman, A. P., Tan, X., & Parmentier, V. 2020, Space Science Reviews, 216, 139
Showman, A. P., Tan, X., & Zhang, X. 2019, The Astrophysical Journal, 883, 4
Sing, D. K., Rustamkulov, Z., Thorngren, D. P., et al. 2024, Nature [arXiv:2405.11027]
Steinrueck, M. E., Parmentier, V., Showman, A. P., Lothringer, J. D., & Lupu, R. E. 2019, The Astrophysical Journal, 880, 14
Sumlin, B. J., Heinson, W. R., & Chakrabarty, R. K. 2018, Journal of Quantitative Spectroscopy and Radiative Transfer, 205, 127
Tan, X. & Showman, A. P. 2019, The Astrophysical Journal, 874, 111
Tan, X. & Showman, A. P. 2021a, Monthly Notices of the Royal Astronomical Society, 502, 678
Tan, X. & Showman, A. P. 2021b, Monthly Notices of the Royal Astronomical Society, 502, 2198
Taylor, J., Parmentier, V., Line, M. R., et al. 2021, Monthly Notices of the Royal Astronomical Society, 506, 1309
Thorngren, D., Gao, P., & Fortney, J. J. 2019, ApJ, 884, L6
Triaud, A. H. M. J., Anderson, D. R., Collier Cameron, A., et al. 2013, A&A, 551, A80
Triaud, A. H. M. J., Dransfield, G., Kagetani, T., et al. 2023, Monthly Notices of the Royal Astronomical Society: Letters, 525, L98
Tsai, S.-M., Malik, M., Kitzmann, D., et al. 2021, The Astrophysical Journal, 923, 264
Veillet, R., Venot, O., Sirjean, B., et al. 2025, Inclusion of Sulfur Chemistry in a Validated C/H/O/N Chemical Network: Identification of Key C/S Coupling Pathways
Visscher, C., Lodders, K., & Fegley, B. 2010, The Astrophysical Journal, 716, 1060
Visscher, C., Lodders, K., & Fegley, Jr., B. 2006, The Astrophysical Journal, 648, 1181
Wang, H. & Wordsworth, R. 2020, The Astrophysical Journal, 891, 7
Wardenier, J. P., Parmentier, V., Lee, E. K. H., Line, M. R., & Gharib-Nezhad, E. 2021, Monthly Notices of the Royal Astronomical Society, 506, 1258
Welbanks, L., Bell, T. J., Beatty, T. G., et al. 2024, Nature [arXiv:2405.11018]
Wiser, L. S., Bell, T. J., Line, M. R., et al. 2025, Proceedings of the National Academy of Sciences, 122, e2416193122
Wiser, L. S., Line, M. R., Welbanks, L., et al. 2024, The Astrophysical Journal, 971, 33
Zamyatina, M., Christie, D. A., Hébrard, E., et al. 2024, 529, 1776
Zamyatina, M., Hébrard, E., Drummond, B., et al. 2022, Monthly Notices of the Royal Astronomical Society, 519, 3129
Zhang, J., Kempton, E. M. R., & Rauscher, E. 2017, The Astrophysical Journal, 851, 84

Appendix A: Atmosphere of WASP-80b

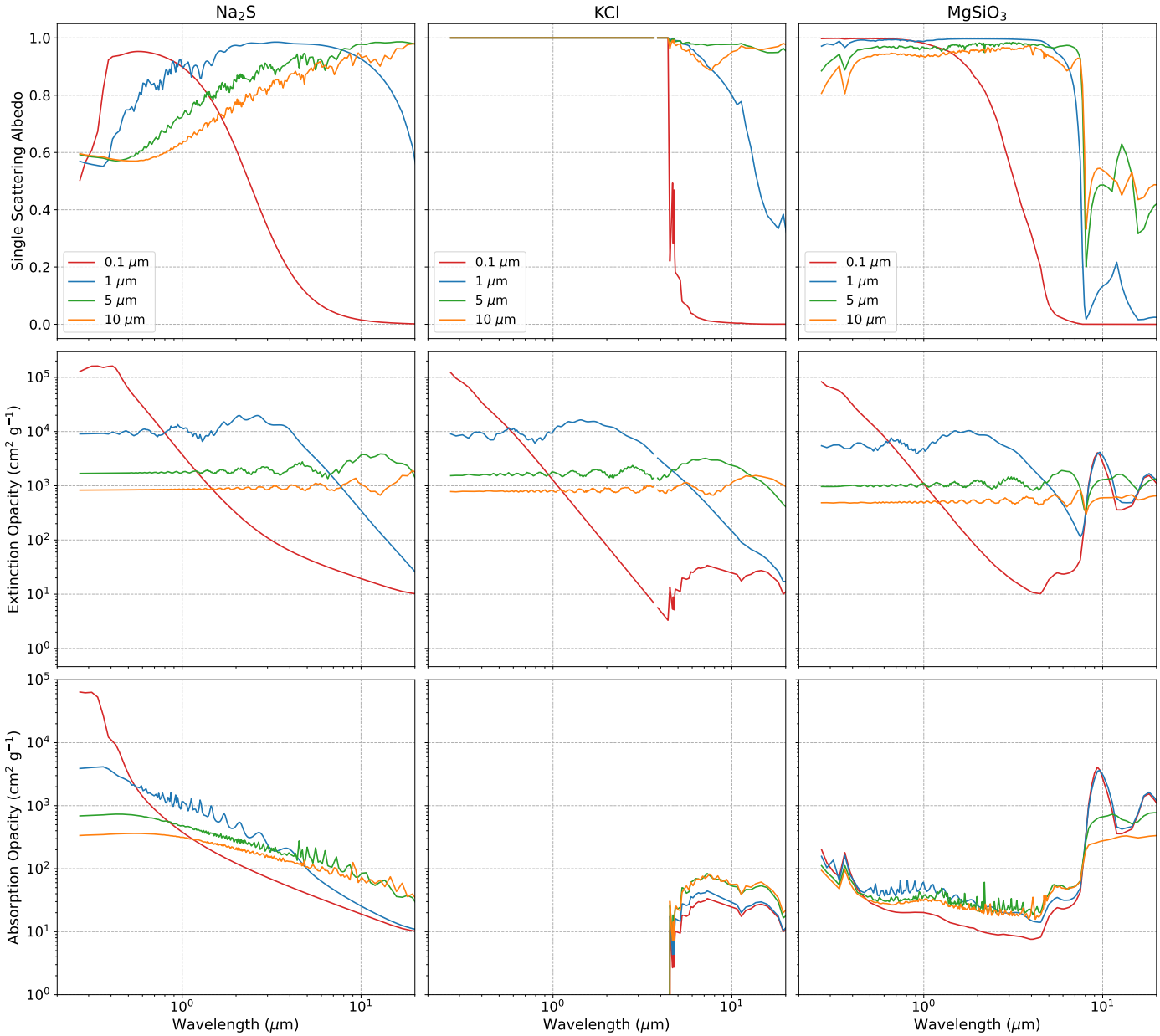

Fig. A.1. Wavelength-dependent single scattering albedo (top row), extinction opacity (middle row), and absorption opacity (bottom row) for Na_2S (left), KCl (middle), and $MgSiO_3$ (right) clouds. They are calculated for particle radii of 0.1, 1.0, 5.0, and 10.0 μm using *PyMieScatt* (Sumlin et al. 2018).

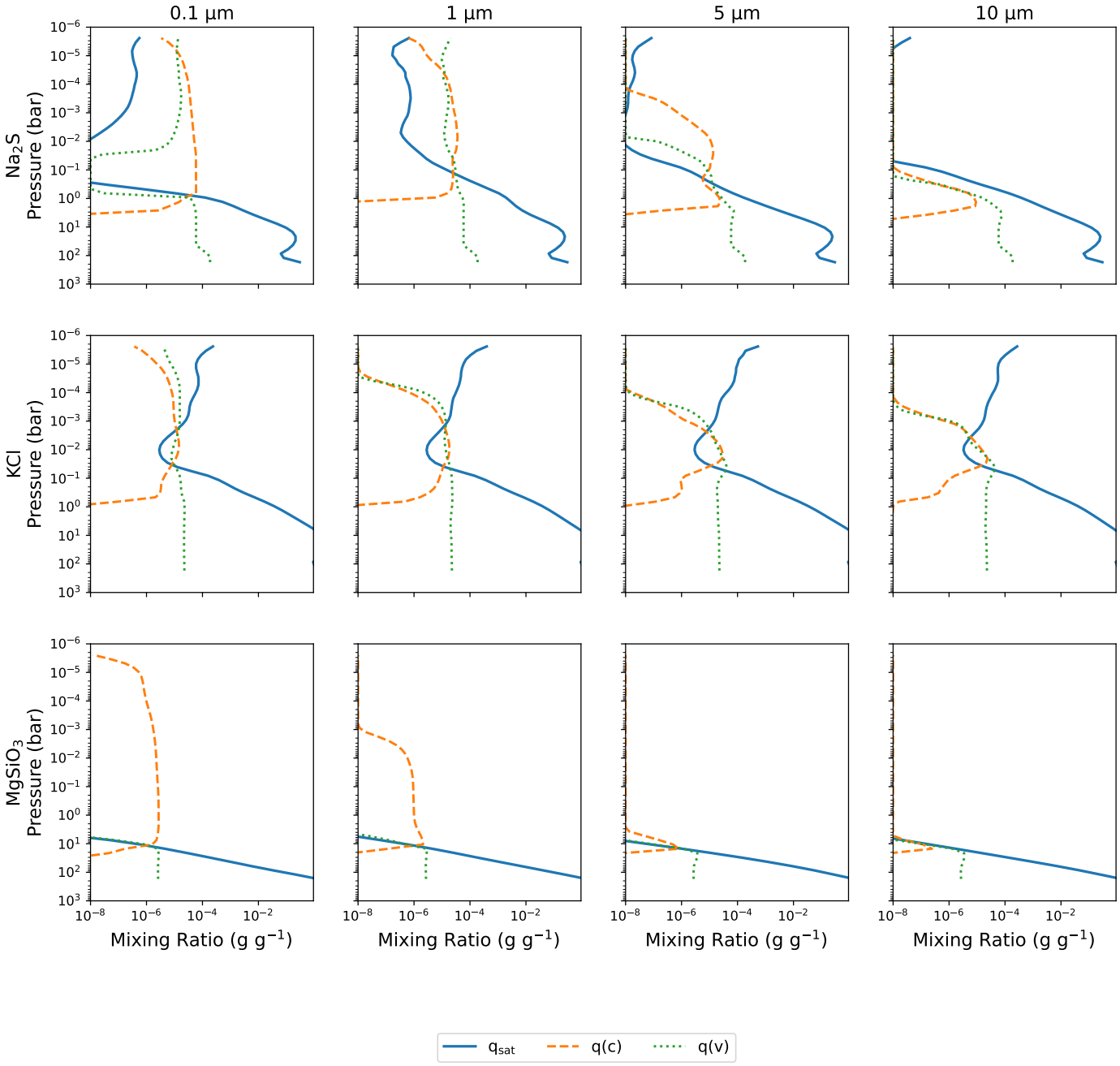

Fig. A.2. Globally-averaged mass mixing of condensate (q_c) and vapor (q_v) compared with saturation mixing ratio (q_{sat}). The columns show the radii of the cloud particle (0.1, 1, 5, 10 μm) and the rows show the cloud species (Na_2S, KCl, $MgSiO_3$)

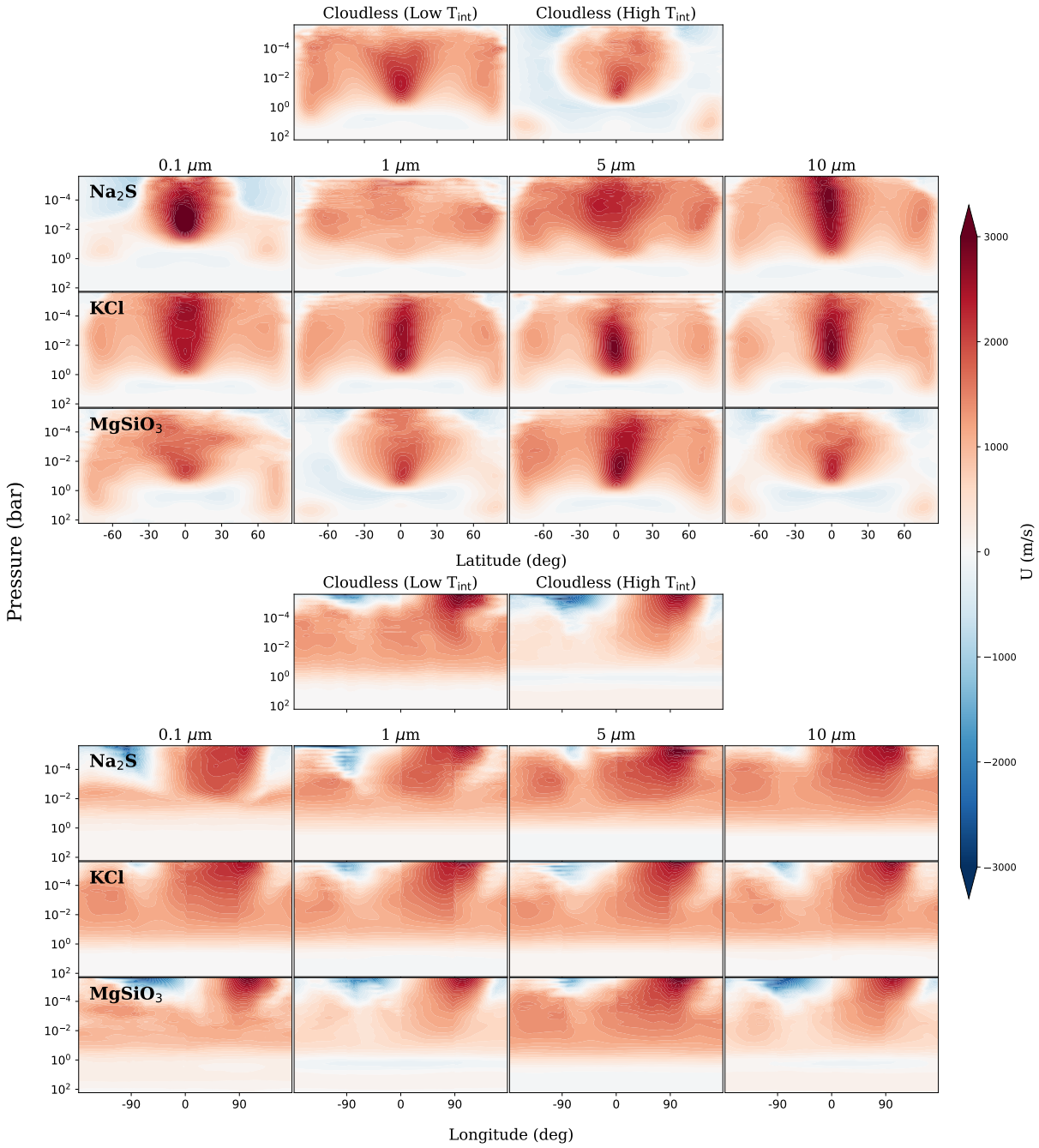

Fig. A.3. Same as Fig. 5 but for Zonal component of wind.

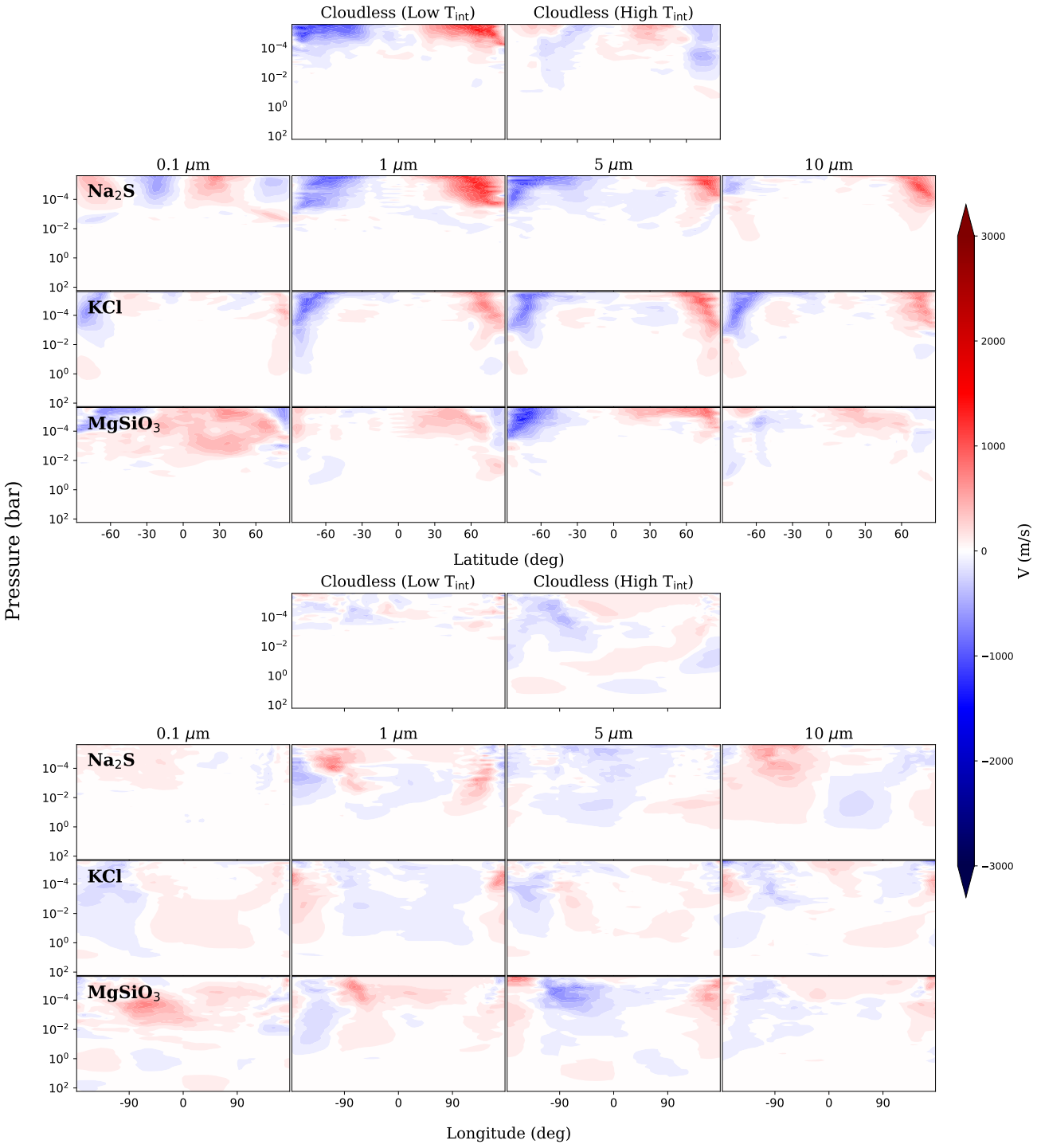

Fig. A.4. Same as Fig. 5 but for Meridional component of wind.

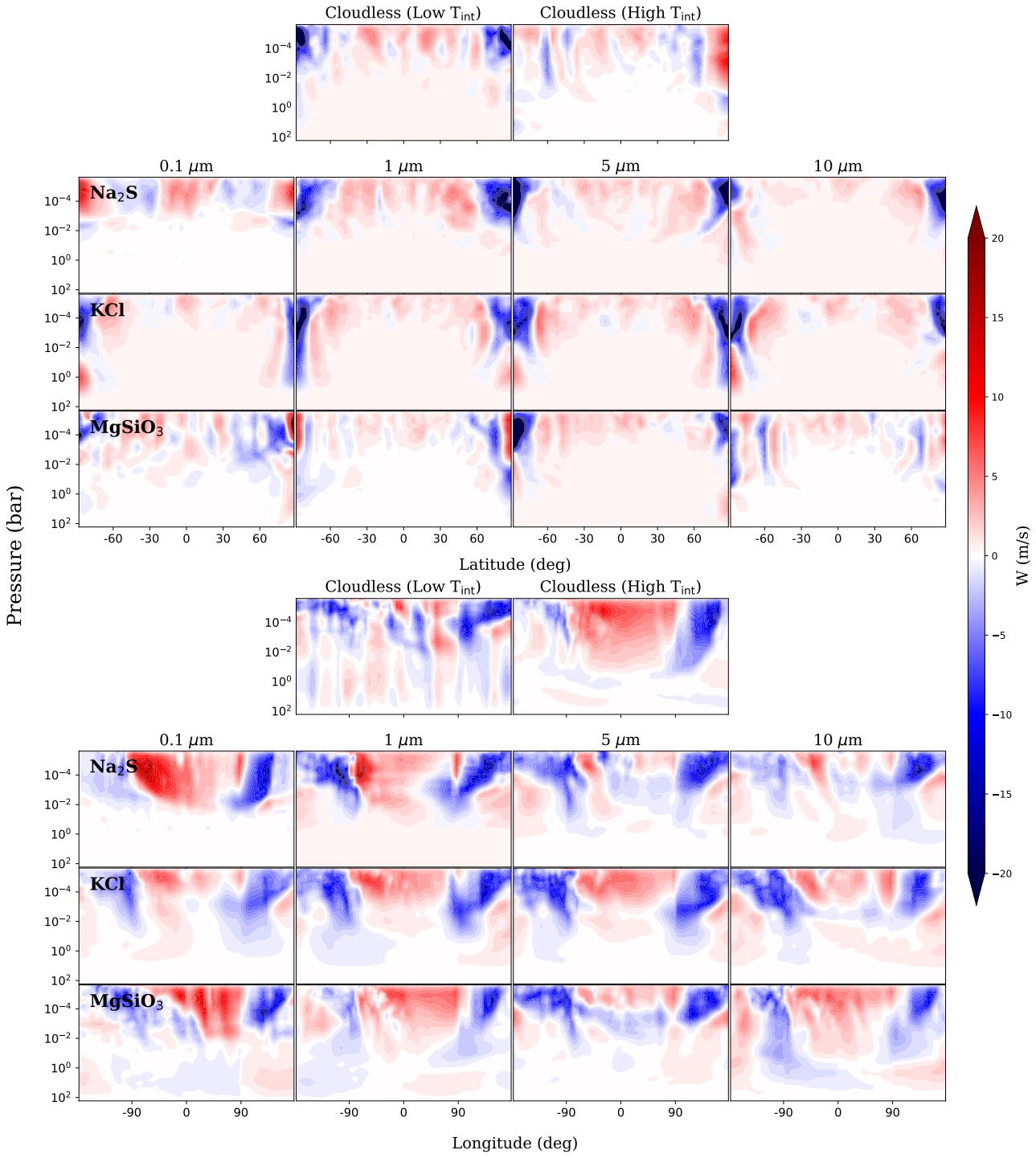

Fig. A.5. Same as Fig. 5 but for Vertical component of wind.

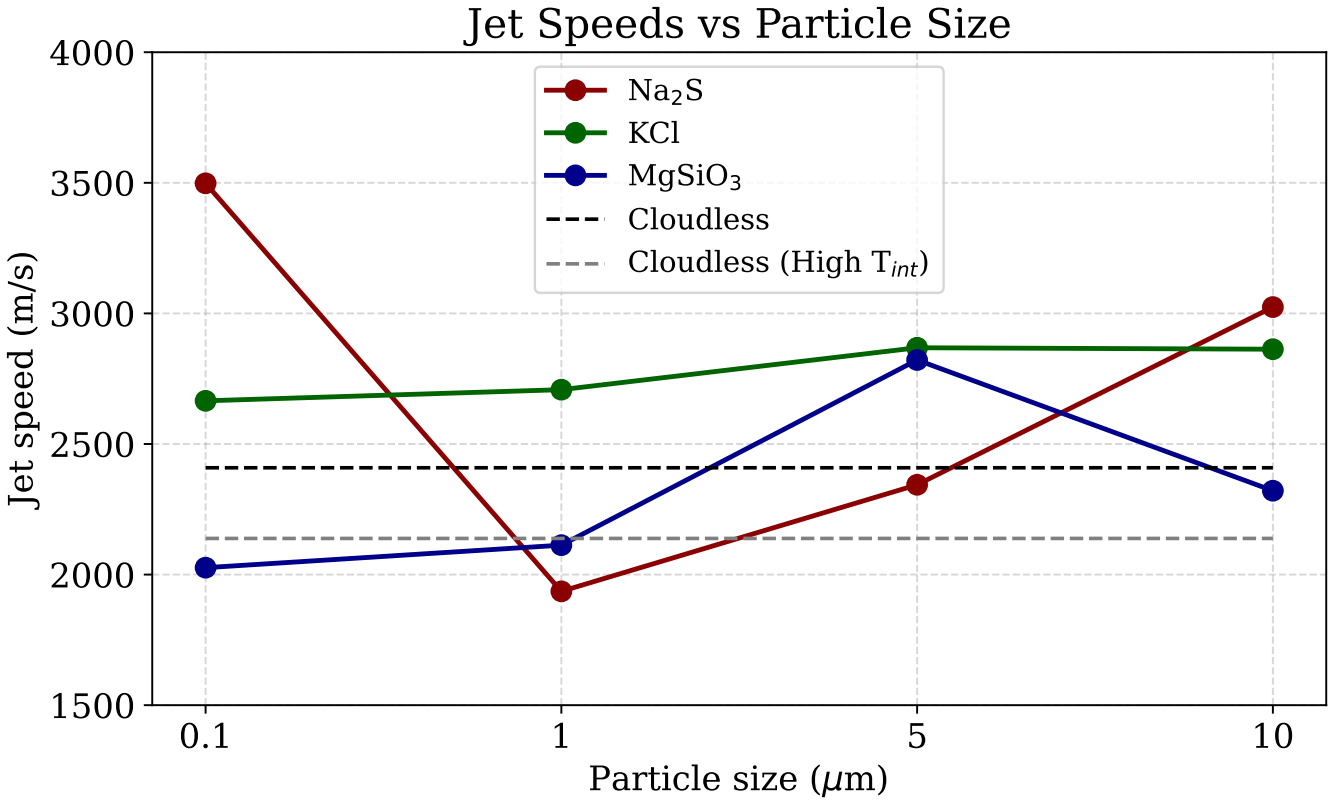

Fig. A.6. Jet speed (Maximum zonal-mean zonal wind speed) as a function of cloud particle size, shown for each cloud species considered in the study. This plot illustrates how the characteristic particle radius influences the strength of the atmospheric jets, highlighting differences in dynamical behavior associated with Na_2S, KCl, and $MgSiO_3$ clouds.

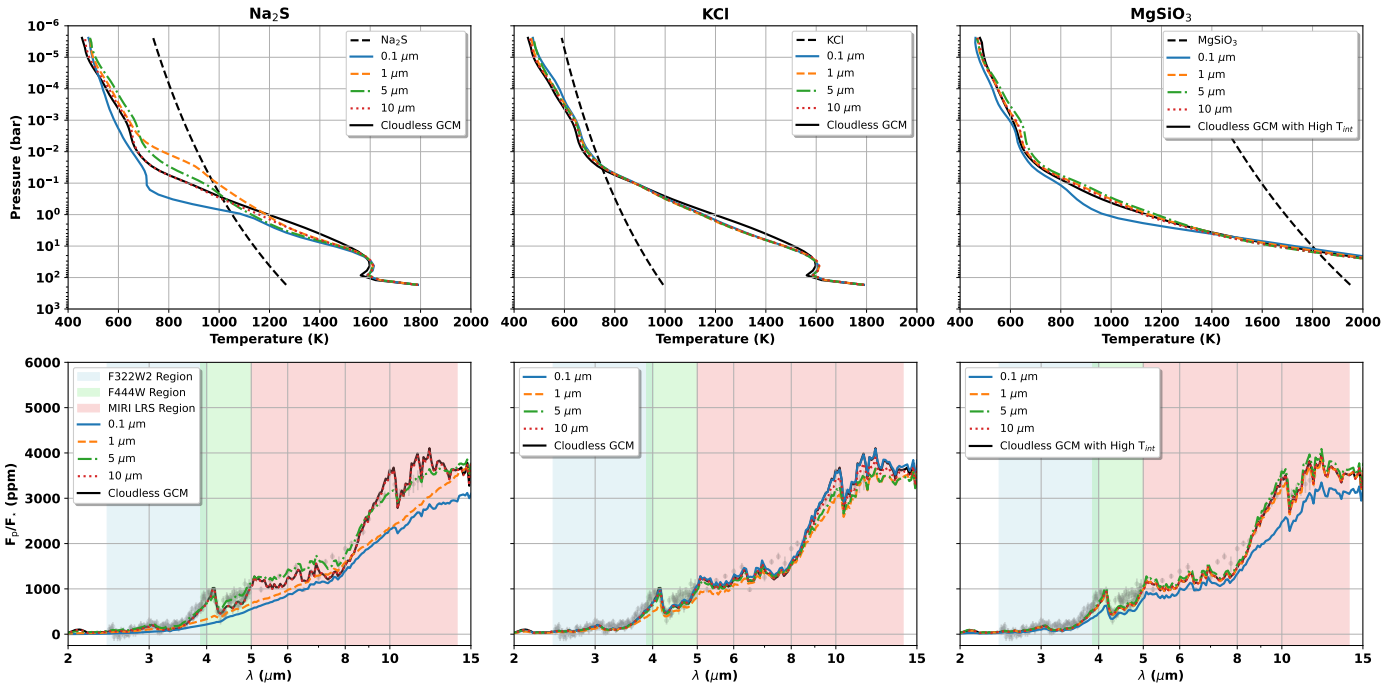

Fig. A.7. Top Row: Nightside averaged Pressure-Temperature profiles for different particle sizes along with the cloudless case (solid black line). The condensation curve for the corresponding cloud species is plotted with a black line. Bottom Row: Emission Spectra from GCM models along with the cloudless case (solid black line) and the dayside JWST observation (grey).